

1 **Constraining frequency-magnitude-area relationships for rainfall and flood**
2 **discharges using radar-derived precipitation estimates: Example applications in the**
3 **Upper and Lower Colorado River Basins, U.S.A.**

4 Caitlin A. Orem*, Jon D. Pelletier

5 [1] {Department of Geosciences, The University of Arizona, 1040 E. 4th Street, Tucson,
6 AZ 85721, USA}

7 Correspondence to: C.A. Orem (oremc@email.arizona.edu)

8

9 **Abstract**

10 Flood-envelope curves (FEC) are useful for constraining the upper limit of possible flood
11 discharges within drainage basins in a particular hydroclimatic region. Their usefulness,
12 however, is limited by their lack of a well-defined recurrence interval. In this study we
13 use radar-derived precipitation estimates to develop an alternative to the FEC method, i.e.
14 the frequency-magnitude-area-curve (FMAC) method, that incorporates recurrence
15 intervals. The FMAC method is demonstrated in two well-studied U.S. drainage basins,
16 i.e. the Upper and Lower Colorado River basins (UCRB and LCRB, respectively), using
17 Stage III Next-Generation-Radar (NEXRAD) gridded products and the diffusion-wave
18 flow-routing algorithm. The FMAC method can be applied worldwide using any radar-
19 derived precipitation estimates. In the FMAC method, idealized basins of similar
20 contributing area are grouped together for frequency-magnitude analysis of precipitation
21 intensity. These data are then routed through the idealized drainage basins of different
22 contributing areas, using contributing-area-specific estimates for channel slope and
23 channel width. Our results show that FMACs of precipitation discharge are power-law
24 functions of contributing area with an average exponent of 0.82 ± 0.06 for recurrence
25 intervals from 10 to 500 years. We compare our FMACs to published FECs and find that
26 for wet antecedent-moisture conditions, the 500-year FMAC of flood discharge in the
27 UCRB is on par with the U.S. FEC for contributing areas of $\sim 10^2$ to 10^3 km^2 . FMACs of
28 flood discharge for the LCRB exceed the published FEC for the LCRB for contributing
29 areas in the range of $\sim 10^3$ to 10^4 km^2 . The FMAC method retains the power of the FEC
30 method for constraining flood hazards in basins that are ungauged or have short flood

31 records, yet it has the added advantage that it includes recurrence interval information
32 necessary for estimating event probabilities.

33

34 **1. Introduction**

35 **1.1 Flood-Envelope Curves**

36 For nearly a century, the flood-envelope curves (FEC), i.e. a curve drawn slightly
37 above the largest measured flood discharges on a plot of discharge versus contributing
38 area for a given hydroclimatic region (Enzel et al., 1993), have been an important tool for
39 predicting the magnitude of potential future floods, especially in regions with limited
40 stream-gauge data. FECs assume that, within a given hydroclimatic region, maximum
41 flood discharges for one drainage basin are similar to those of other drainage basins of
42 the same area, despite differences in relief, soil characteristics, slope aspect, etc. (Enzel et
43 al., 1993). This assumption enables sparse and/or short-duration flood records over a
44 hydroclimatic region to be aggregated in order to provide more precise constraints on the
45 magnitude of the largest possible (i.e. long-recurrence-interval) floods.

46 FECs reported in the literature have a broadly similar shape across regions of
47 widely differing climate and topography. For example, FECs for the Colorado River
48 Basin (Enzel et al., 1993), the central Appalachian Mountains (Miller, 1990; Morrison
49 and Smith, 2002), the 17 hydrologic regions within the U.S. defined by Crippen and Bue
50 (1977), the U.S. as a whole (Costa, 1987; Herschy, 2002), and China (Herschy, 2002) are
51 all concave-down when plotted in log-log space, with maximum recorded flood
52 discharges following a power-law function of contributing area for small contributing
53 areas and increasing more slowly at larger contributing areas (i.e. the curve “flattens”).

54 Traditional FECs also have the potential problem that the maximum flood
55 associated with smaller drainage basins may be biased upward (or the floods of larger
56 drainage basins biased downward) because there are typically many more records of
57 floods in smaller drainage basins relative to larger drainage basins (because there are
58 necessarily fewer large drainage basins in any hydroclimatic region). That is, the largest
59 flood of record for small drainage basins within a hydroclimatic region likely corresponds
60 to a flood of a larger recurrence interval compared with the largest flood of record for
61 larger drainage basins. In this paper we present a method that includes recurrence-interval

62 information and avoids any sample-size bias that might exist as a function of contributing
63 area.

64 The use of FECs to quantify flood regimes is limited by the lack of recurrence-
65 interval information (Wolman and Costa, 1984; Castellarin et al., 2005) and by the short
66 length, incomplete nature, and sparseness of many flood discharge records. Without
67 recurrence-interval information, the data provided by FECs are difficult to apply to some
68 research and planning questions related to floods. In the U.S. for example, the 100- and
69 500-year flood events are the standard event sizes that define flood risk for land planning
70 and engineering applications (FEMA, 2001).

71 Previously published studies have looked at new approaches to approve upon the
72 FEC method. Castellarin et al. (2005) took a probabilistic approach to estimating the
73 exceedance probability of the FEC for synthetic flood data. The authors were able to
74 relate the FECs of certain recurrence intervals to the correlation between sites, the
75 number of flood observations, and the length of each observation. Later, Castellarin
76 (2007) and Castellarin et al. (2009) applied these methods to real flood record data and
77 extreme rainfall events for basins within north-central Italy. Castellarin et al. (2009) also
78 created depth-duration envelope curves of precipitation to relate extreme precipitation
79 events to mean annual precipitation. This group of studies was successful in
80 incorporating recurrence-interval information into the traditional FEC method. However,
81 most of the models presented in these studies were completed with synthetic data or
82 created for design storm processes and require additional analysis. Also, most of the
83 precipitation data used in these past studies was collected using rain gauges (point
84 sources), while only a small subset of data in Castellarin et al. (2009) was sourced from
85 radar-derived precipitation estimates. In contrast to these studies we formulate a
86 simplified method (i.e. the FMAC method) that is readily applicable to any region of
87 interest and can be directly compared to already existing FECs. Also we favor the use of
88 spatially complete radar-derived precipitation estimates in order to apply our methods to
89 ungauged basins.

90 To mitigate the uncertainty caused by short and incomplete flood discharge
91 records, this study uses a space-for-time substitution (e.g. regionalization) to lengthen the
92 record for a given contributing area. Previous studies have employed similar methods,

93 including the index-flood procedure first described by Dalyrymple (1960) and expanded
94 upon by many subsequent authors. The index-flood method uses data from multiple sites
95 within a region to construct more accurate flood-quantile estimates than would be
96 possible using a single site (Stedinger et al., 1993 and Hosking and Wallis, 2005). This
97 method can also be used on precipitation data where it is referred to as the station-year
98 method (Buishand, 1991). The index-flood method is based on two major assumptions:
99 (1) that observations from two or more basins are independent; and (2) that observations
100 follow the same distribution (Wallis et al., 2007).

101 Here we use a regionalization method similar to the index-flood method in order
102 to calculate rainfall intensity values associated with specific recurrence intervals. The
103 assumption of statistical independence of rainfall (and associated flood) observations is
104 one that we assume in this study but understand may not be true for all samples in our
105 natural data set. This assumption is difficult to definitively prove with natural data
106 (Hosking and Wallis, 2005). For example, a large rainfall event may affect two basins in
107 a similar way and therefore create correlated maximum rainfall intensity values. This
108 spatial correlation is difficult to avoid and may cause biased results. However, it has been
109 shown that the index-flood method can be used in the absence of fully statistically
110 independent observations and still give robust results (Hosking and Wallis, 1988;
111 Hosking and Wallis, 2005). The assumption that observations are sampled from the same
112 distribution is also somewhat difficult to prove with natural data, but by knowing the
113 study areas well a researcher can identify regions with similar rainfall and flood
114 mechanisms. Many examples of this type of area analysis can be found in the literature,
115 including Soong et al. (2004) who separated rural streams in Illinois into hydrological
116 regions based on basin morphology and soil characteristics. Soong et al. (2004) used
117 regionalization in their study to increase the amount of flood data available for frequency
118 analysis. Wallis et al. (2007) employed a similar regionalization method to identify
119 hydroloclimatic regions in their study of precipitation frequency in Washington. It should
120 be noted that FEC's in general use this type of regionalization approach to analyze
121 maximum flood data for hydroclimatic regions with similar flood mechanisms. In this
122 study we similarly attempt to analyze regions based on their basic rainfall mechanisms, in
123 this case by separating the Upper and Lower Colorado River basins.

124 In this study, a new method for estimating flood discharges associated with user-
125 specified recurrence intervals is introduced that uses radar-derived precipitation estimates
126 (in this case rainfall only), combined with the diffusion-wave flow-routing algorithm, to
127 create frequency-magnitude-area curves (FMACs) of flood discharge. Our method (i.e.
128 the FMAC method) retains the power of the FEC approach in that data from different
129 drainage basins within a hydroclimatic region are aggregated by contributing area,
130 thereby enabling large sample sizes to be obtained within each contributing-area class in
131 order to more accurately constrain the frequencies of past extreme flood events and hence
132 the probabilities of future extreme flood events within each class. The method improves
133 upon the FEC approach in that the complete spatial coverage of radar-derived
134 precipitation estimates provides for large sample sizes of most classes of contributing
135 area (larger contributing areas have fewer samples). The radar-derived precipitation
136 estimates include only rainfall and therefore snow and other types of precipitation are not
137 included in the study. The precipitation estimates are then used to predict flood
138 discharges associated with specific recurrence intervals by first accounting for water lost
139 to infiltration and evapotranspiration using runoff coefficients appropriate for different
140 contributing areas and antecedent-moisture conditions, and then routing the available
141 water using a flow-routing algorithm. Predicted flood discharges are presented as FMACs
142 on log-log plots, similar to traditional FECs, except that the method predicts a family of
143 curves, one for each user-defined recurrence interval. These plots are then compared to
144 FECs for the study region (Enzel et al., 1993) and the U.S. (Costa, 1987).

145

146 **1.2 Study Area**

147 This study focuses on the Upper and Lower Colorado River Basins (UCRB and
148 LCRB, respectively; Fig. 1) as example applications of the FMAC method. Although the
149 methods we develop are applied to the UCRB and LCRB in the western U.S. in this
150 study, the methods are applicable to any region of interest where radar-derived
151 precipitation estimates are available (i.e. the entire U.S. and at least 22 countries around
152 the world; Li, 2013; RadarEU, 2014). We focus on the UCRB and LCRB because they
153 have been a focus of flood-hazard assessment studies in the western U.S. and hence the
154 FECs available for them are of especially high quality. In addition, the distinctly different

155 hydroclimatic regions of the UCRB and LCRB (Sankarasubramanian and Vogel, 2003)
156 make working in these regions an excellent opportunity to test and develop the new
157 methods of this study on different precipitation patterns and storm types.

158 Precipitation and flooding in the LCRB are caused by convective-type storms,
159 including those generated by the North American Monsoon (NAM), and frontal-type and
160 tropical storms sourced from the Pacific Ocean and the Gulf of California (House and
161 Hirschboeck, 1997; Etheredge et al., 2004). In the UCRB, the influence of the NAM and
162 tropical storms is diminished and floods are generally caused by Pacific frontal-type
163 storms (Hidalgo and Dracup, 2003). In both regions, the El Niño Southern Oscillation
164 (ENSO) alters the frequency and intensity of the NAM, tropical storms, and the Pacific
165 frontal systems, and can cause annual variations in precipitation and flooding (House and
166 Hirschboeck, 1997; Hidalgo and Dracup, 2003). Winter storms in both regions are also
167 intensified by the occurrence of atmospheric rivers (Dettinger et al., 2011), which can
168 cause total winter precipitation to increase up to approximately 25% (Rutz and
169 Steenburgh, 2012). The radar-derived precipitation estimates used in this study record
170 this natural variability in precipitation in the two regions.

171 The methods used in this study to calculate rainfall and flood discharges of
172 specified recurrence intervals from radar-derived precipitation estimates require a few
173 main assumptions. The first assumption is that of climate stationarity, i.e. the parameters
174 that define the distribution of floods do not change through time (Milly et al., 2008).
175 Climate is changing and these changes pose a challenge to hazard predictions based on
176 the frequencies of past events. Nevertheless, stationarity is a necessary assumption for
177 any probabilistic analysis that uses past data to make future predictions. The results of
178 such analyses provide useful starting points for more comprehensive analyses that
179 include the effects of future climate changes. The second assumption is that the sample
180 time interval is long enough to correctly represent the current hydroclimatic state (and its
181 associated precipitation patterns and flood magnitudes and risks) of the specified study
182 area. Our study uses data for the 1996 to 2004 water years and therefore may be limited
183 by inadequate sampling of some types of rare weather patterns and climate fluctuations
184 within that time interval. To address whether or not the sample time interval used in this
185 study includes major changes in circulation and weather patterns, and therefore is a good

186 representation of climate in the CRB, we investigated the effect of the El Niño Southern
187 Oscillation (ENSO) on rainfall intensity within the UCRB and LCRB. ENSO is a well-
188 known important influence on the hydroclimatology of the western U.S. (Hidalgo and
189 Dracup, 2003; Cañon et al., 2007). In general, winter precipitation in the southwestern
190 U.S. increases during El Niño events and decreases during La Niña events (Hidalgo and
191 Dracup, 2003). The opposite effects are found in the northwestern portions of the U.S.
192 (including the UCRB; Hidalgo and Dracup, 2003). The last assumption of the method is
193 that all basins of similar contributing area respond similarly to input rainfall, i.e. that they
194 have similar flood-generating and flow-routing mechanisms. Specifically, the method
195 assumes that basins of similar contributing area have the same runoff coefficient, flow-
196 routing parameters, basin shape, and channel length, width, and slope. This assumption is
197 necessary in order to aggregate data into discrete contributing-area classes so that the
198 frequency of extreme events can be estimated from relatively short-duration records. In
199 this study, high-recurrence-interval events (i.e. low frequency events) can be considered
200 despite the relatively short length of radar-derived-precipitation-estimate records because
201 the number of samples in the radar-derived record is extremely large, especially for small
202 contributing areas and small duration floods. For example, for a 1-h time-interval-of-
203 measurement and a contributing area of 4,096 km² event in the UCRB, there are
204 approximately 40 (number of spatial scale samples) times 55000 (number of temporal
205 scale samples in nine years of data) samples of rainfall-intensity values (and associated
206 modeled discharges obtained via flow routing). As contributing area and time intervals of
207 measurement increase there are successively fewer samples, within any particular
208 hydroclimatic region, thus increasing the uncertainty of the resulting probability
209 assessment for larger areas and longer time periods.

210

211 2. Next-Generation-Radar (NEXRAD) Data

212 The specific radar-derived precipitation estimates we use in this study come from
213 the Stage III Next-Generation-Radar (NEXRAD) gridded product, which is provided for
214 the entire U.S., Guam, and Puerto Rico. NEXRAD was introduced in 1988 with the
215 introduction of the Weather Surveillance Radar 1988 Doppler, or WSR-88D, network
216 (Fulton et al., 1998). The WSR-88D radars use the Precipitation Processing System

217 (PPS), a set of automated algorithms, to produce precipitation intensity estimates from
218 reflectivity data. Reflectivity values are transformed to precipitation intensities through
219 the empirical Z - R power-law relationship,

220
$$Z = \alpha R^\beta \quad (1)$$

221 where Z is precipitation rate (mm h^{-1}), α and β are derived empirically and can vary
222 depending on location, season, and other conditions (Smith and Krajewski, 1993), and R
223 is reflectivity ($\text{mm}^6 \text{ m}^{-3}$; Smith and Krajewski, 1993; Fulton et al., 1998; Johnson et al.,
224 1999). Precipitation intensity data are filtered and processed further to create the most
225 complete and correct product (Smith and Krajewski, 1993; Smith et al., 1996; Fulton et
226 al., 1998; Baeck and Smith, 1998). Further information and details about PPS processing
227 are thoroughly described by Fulton et al. (1998).

228 Stage III NEXRAD gridded products are Stage II precipitation products mapped
229 onto the Hydrologic Rainfall Analysis Project (HRAP) grid (Shedd and Fulton, 1993).
230 Stage II data are hourly precipitation intensity products that incorporate both radar
231 reflectivity and rain-gauge data (Shedd and Fulton, 1993) in an attempt to make the most
232 accurate precipitation estimates possible. The HRAP grid is a polar coordinate grid that
233 covers the conterminous U.S., with an average grid size is 4 km by 4 km, although grid
234 size varies from approximately 3.7 km (north to south) to 4.4 km (east to west) in the
235 southern and northern U.S., respectively (Fulton et al., 1998).

236

237 **3. Methods**

238 **3.1 NEXRAD Data Conversion and Sampling**

239 NEXRAD Stage III gridded products (hereafter NEXRAD products) for an area
240 covering the Colorado River basin from 1996 to 2005 were downloaded from the NOAA
241 HDSG website (http://dipper.nws.noaa.gov/hdsb/data/nexrad/cbrfc_stageiii.php) for
242 analysis. The data files were converted from archived XMRG files to ASCII format (each
243 data file representing the mean rainfall intensity within each 1 h interval) using the
244 xmrptoasc.c program provided on the NOAA HDSG website. The ASCII data files were
245 then input into a custom program written in IDL for analysis.

246

247 **3.2 Rainfall Sampling Over Space**

248 In this study we quantified hourly rainfall intensities (mm h⁻¹) over square
249 idealized drainage basins (i.e. not real drainage basins, but square drainage basins as
250 shown schematically in Fig. 2A as brown squares) of a range of areas from 16 km² to
251 11,664 km² (approximately the contributing area of the Bill Williams River, AZ, for
252 readers familiar with the geography of the western U.S.) by successively spatially
253 averaging rainfall-intensity values at HRAP pixel-length scales of powers of two (e.g. 4,
254 16 pixel², etc.) and three (e.g. 9, 81 pixel², etc.; Fig. 2, Step 1). Spatial averaging is done
255 by both powers of 2 and 3 simply to include more points on the FMACs than would
256 result from using powers of 2 or 3 alone. The number of samples within each contributing
257 area class limited the range of contributing areas used in this study, i.e. at larger
258 contributing areas there were too few samples to successfully apply the frequency
259 analysis.

260 UCRB and LCRB boundaries from GIS hydrologic unit layers created by the
261 USGS and provided online through the National Atlas site
262 (<http://www.nationalatlas.gov/atlasftp.html#hucs00m>) were projected to HRAP
263 coordinates using the methods of Reed and Maidment (2006). These boundaries were
264 used to delineate the region from which rainfall data were sampled from the NEXRAD
265 products, i.e. when averaging rainfall data by powers of two and three a candidate square
266 drainage basin was not included in the analysis if any portion of the square fell outside of
267 the boundaries of the UCRB or LCRB (Fig. 2A). Throughout the analysis, the HRAP
268 pixel size was approximated by a constant 4 km by 4 km size despite the fact that HRAP
269 pixel sizes vary slightly as a function of latitude (Reed and Maidment, 2006). Our study's
270 drainage basins span latitudes between approximately 31°N and 43°N resulting in a
271 maximum error of 15%. However, by keeping the pixel size constant, all pixels could be
272 treated as identical in size and shape allowing us to sample the NEXRAD products in an
273 efficient and automated way over many spatial scales.

274 For larger contributing areas, necessarily fewer samples are available within a
275 given hydroclimatic region, thus increasing the uncertainty associated with the analysis
276 for those larger contributing-area classes. For the UCRB and LCRB specifically, the
277 uncertainty in the analysis becomes significant for contributing-area classes equal to and
278 larger than $\sim 10^3$ to 10^4 km² depending on the recurrence interval being analyzed. Of

279 course, if the hydroclimatic region is defined to be larger, more samples are available for
280 each contributing-area class and hence larger basins can be analyzed with confidence.

281

282 **3.3 Rainfall Sampling Over Time**

283 In addition to computing rainfall intensities as a function of spatial scale, we
284 averaged rainfall intensities as a function of the time interval of measurement ranging
285 from 1 to 64 hours in powers of two by averaging hourly rainfall intensity records over
286 the entire 9-year study period (Fig. 2, Step 1). This range in time intervals was chosen in
287 order to capture rainfall events that last on the order of ~1 hour (convective-type storms)
288 to days (frontal-type storms).

289 Rainfall data was sampled temporally by taking the maximum value of each storm
290 event. Storm events were identified as consecutive non-zero rainfall intensity values
291 separated by instances of zero values in time for each temporal scale. This allows for
292 multiple maximum rainfall values in time to be sampled within a year and throughout the
293 entire 9-year study period. This sampling method is similar to that used in the Peak Over
294 Threshold (POT) method typically used on discharge data where a minimum threshold
295 value is set and maximum peaks above the threshold value are recorded as maximum
296 events. Here we set the minimum threshold value to zero and hence the maximum values
297 of all individual storm events are considered in the analysis.

298

299

300 **3.4 Rainfall Recurrence Interval Calculations**

301 To determine the rainfall-intensity values with a user-specified recurrence
302 interval, maximum rainfall intensities of storm events sampled from the NEXRAD data
303 for each contributing-area and time-interval-of-measurement class were first ranked from
304 highest to lowest (Fig. 2A, Step 2). The relationship between recurrence intervals and
305 rank in the ordered list is given by the probability-of-exceedance equation (i.e. the
306 frequency-rank relationship):

$$307 RI = \frac{(n+1)}{m} \quad (2)$$

308 where RI is the recurrence interval (yr), defined as the inverse of frequency (yr^{-1}) or
309 probability of exceedance, n is the total number of samples in each contributing-area and
310 time-interval-of-measurement scaled to units in years (resulting in units of yr), and m is
311 the rank of the magnitude ordered from largest to smallest (unitless). Here the recurrence
312 interval is prescribed (10, 50, 100, and 500 yr), then the rank associated with this
313 recurrence interval is computed using the frequency-rank relationship (Equation 2). The
314 resulting rainfall intensities associated with a user-specified recurrence interval and
315 contributing-area and time-interval-of-measurement class was then used to calculate the
316 Q_p value.

317 At the end of the calculations described above we have datasets of rainfall-
318 intensity values for each combination of the eight contributing-area classes, the seven
319 time-interval-of-measurement classes, and the four recurrence intervals. We then find the
320 maximum values of rainfall intensity associated with a given contributing-area class and
321 recurrence interval among all values of the time-interval-of-measurement class (i.e. the
322 values calculated for 1 to 64 h time intervals). This step is necessary in order to find the
323 maximum values for a given contributing area class and recurrence interval independent
324 of the time-interval-of-measurement, i.e. independent of storm durations and associated
325 types of storms. The maximum values are used to be consistent with the methods of the
326 traditional FECs where the points represent the largest possible storm for a given
327 contributing area. These maximum values are used to calculate Q_p and Q_{fd} (see next
328 section).

329

330 **3.5 Rainfall and Runoff Calculations**

331 The first variable calculated from the maximum rainfall intensities found for each
332 contributing-area class and recurrence interval is the precipitation (here rainfall only)
333 discharge, Q_p . The variable Q_p is defined as the average rainfall intensity over a basin and
334 time interval of measurement multiplied by the contributing area, resulting in units of m^3
335 s^{-1} . This is a simple calculation resulting in a “discharge” of rainfall to a basin. Q_p is the
336 input value for the flow-routing algorithm that we employ to calculate the peak flood
337 discharge (Fig. 2B, Step 3).

338 The flow-routing algorithm we employ does not explicitly include infiltration and
339 other losses that can further reduce peak flood discharge relative to input to the basin, Q_p .
340 In this study we modeled infiltration and evaporation losses by simply removing a
341 volume of water per unit time equal to one minus the runoff coefficient, i.e. the ratio of
342 runoff to rainfall over a specified time interval, for three antecedent-moisture scenarios
343 (wet, med, and dry). We estimated runoff coefficients for each contributing-area class
344 and each of three antecedent-moisture scenarios using published values for annual runoff
345 coefficients for large basins within the UCRB and LCRB (Rosenburg et al., 2013) and
346 published values for event-based runoff coefficients for small basins modeled with a
347 range of antecedent-moisture conditions by Vivoni et al. (2007) (Fig. 3). On average,
348 estimated runoff coefficients are higher for smaller and/or initially wetter basins. We
349 found the dependence of runoff coefficients on contributing area and antecedent moisture
350 to be similar despite the large difference in time scales between event-based and annual
351 values. Despite the difference in geographic region between our study site and that of
352 Vivoni et al. (2007) (they studied basins in Oklahoma), the runoff coefficients they
353 estimated are likely to be broadly applicable to the LCRB and UCRB given that basin
354 size and antecedent moisture are the primary controls on these values (climate and soil
355 types play a lesser role except for extreme cases).

356 We applied the estimated runoff coefficients for all three antecedent-moisture
357 scenarios by simply using them to remove a portion of the Q_p calculated for specific time
358 interval and basin area

359

360
$$Q_{pm} = C * Q_p \quad (3)$$

361

362 where C is the runoff coefficient calculated for the specific basin area and antecedent-
363 moisture scenario under evaluation. The newly formed Q_{pm} is now the Q_p value for the
364 wet, medium, or dry antecedent-moisture scenario under analysis for each given
365 recurrence interval and contributing area class.

366

367 **3.6 Flood Discharge Calculations**

368 The second variable calculated in this study, and the end-result of our methods, is
369 the peak flood discharge, Q_{fd} . The variable Q_{fd} is the peak flood discharge ($m^3 s^{-1}$)
370 calculated via the diffusion-wave flow-routing algorithm for a hypothetical flood
371 triggered by a rainfall discharge, Q_{pm} , input uniformly over the time interval of
372 measurement to idealized square basins associated with each contributing-area class (Fig.
373 2B, Step 4).

374 The flow-routing algorithm routes flow along the main-stem channel of idealized
375 square basins with sizes equal to the contributing area of each contributing-area class.
376 The choice of a square basin is consistent with the square sample areas (see Section 3.1)
377 and it allows for basin shape to remain the same (and therefore comparable) over the
378 range of contributing areas used in this study. The main-stem channel, with a length of L
379 (m), was defined as the diagonal distance from one corner to the opposite corner across
380 the square basin (i.e. L is equal to the square root of two times the area of the square
381 basin). This main-stem channel was used in conjunction with a normalized area function
382 to represent the shape of the basin and the routing of runoff through the drainage basin
383 network. By including the normalized area function, we can account for geomorphic
384 dispersion (i.e. the attenuation of the flood peak due to the fact that rainfall that falls on
385 the landscape will take different paths to the outlet and hence reach the outlet at different
386 times) in our analyses. The normalized area function, $A(x)$ (unitless), is defined as the
387 portion of basin area, $A_L(x)$ (m^2), that contributes flow to the main-stem channel within a
388 given range of distances (x) from the outlet, normalized by the total basin area, A_T (m^2 ;
389 Mesa and Mifflin, 1986; Moussa, 2008). The normalized area function is assumed to be
390 triangular in shape with a maximum value at the midpoint of the main-stem channel from
391 the outlet. Area functions, and related width functions, from real basins used in other
392 studies show this triangular shape in general (Marani et al., 1994; Rinaldo et al., 1995;
393 Veneziano et al., 2000; Rodriguez-Iturbe and Rinaldo, 2001; Puente and Sivakumar,
394 2003; Saco and Kumar, 2008), although not all basins show this shape. The triangular
395 area function has been shown to approximate the average area function of basins and that
396 the peak discharge and time to peak discharge is likely more important to the shape of the
397 flood wave (Henderson, 1963; Rodriguez-Iturbe and Valdes, 1979).

398 A 1-dimensional channel with simplified width and along-channel slope
399 appropriate for channels in the CRB is used to approximate the geometry of the main-
400 stem channel of the idealized basin in the flow-routing algorithm. In addition, values for
401 channel slope, S (m/m), and channel width, w (m), are assigned based on the contributing
402 area of the idealized basin and the results of a least-squares regression to channel-slope
403 and channel-width data from the CRB. We assume here that the assigned channel slopes
404 and widths represent the average value for the entire idealized basin. To find the best
405 approximations for channel slope and width values, we developed formulae that predict
406 average channel slope and channel width as a function of contributing area based on a
407 least-squares fit of the logarithms of slope, width, and contributing area based on
408 approximately 100 sites in the Colorado River Basin (CRB; Fig. 4). The data used in
409 these least-squares regressions included slope, width, and contributing area information
410 from all sites in the LCRB and southern UCRB presented in Moody et al. (2003) and
411 additional sites from USGS stream-gauge sites from across the CRB.

412 The assigned channel slope and width values, together with the values of Q_{pm}
413 modified for each antecedent-moisture scenario, were used to calculate the depth-average
414 velocities, V (m s⁻¹), in hypothetical 1D main-stem channels of idealized square drainage
415 basins corresponding to each contributing-area and time-interval-of-measurement class.
416 In this study, flow velocity is not modeled over space and time, but rather is set at a
417 constant value appropriate for the peak discharge using an iterative approach that solves
418 for the peak depth-averaged flow velocity, uses that velocity to compute the parameters
419 of the diffusion-wave-routing algorithm, routes the flow, and then computes an updated
420 estimate of peak depth-averaged velocity. To calculate the depth-averaged velocity, V , we
421 used Manning's equation, i.e.

$$422 V = \frac{1}{n_M} R^{\frac{2}{3}} S^{\frac{1}{2}}, \quad (4)$$

423 where n_M is Manning's n (assumed to be equal to 0.035), and R is the hydraulic radius
424 (m) calculated with the assigned channel width, and S (m/m) is the assigned channel
425 slope. In order to calculate R , water depth, h , of the peak discharge needed to be
426 determined. In this study h was iteratively solved for based on the peak-flow conditions
427 (i.e. the depth-averaged velocity, V , associated with the peak-flood discharge, Q_{fd}) with h

428 set at 1 m for the first calculation of the flow-routing algorithm. At the end of each
 429 calculation, h is recalculated using Manning's equation. These iterations continue until
 430 the water depth converges on a value (i.e. the change from the last calculation of h to the
 431 next calculation of h is ≤ 0.1 m) corresponding to a specific recurrence interval,
 432 contributing-area class, and time-interval-of-measurement class.

433 The method we used to model flow through the main-stem channel is the
 434 diffusion-wave flow-routing algorithm. This approach is based on the linearized Saint-
 435 Venant equations for shallow-water flow in one dimension. To find a simpler, linear
 436 solution to Saint-Venant equations, Brutsaert (1973) removed the acceleration term from
 437 the equations, leaving the diffusion and advection terms that often provide a reasonable
 438 approximation for watershed runoff modeling (Brutsaert, 1973). Leaving the diffusion
 439 term in the flow-routing algorithm includes hydrodynamic dispersion of the flood wave
 440 in the calculation of the flood hydrograph. In the case where the initial condition is given
 441 by a unit impulse function (Dirac function), the cell response function of the channel, q_d
 442 (units of s^{-1}), is given by:

$$443 \quad q_d = \frac{x}{(2\pi)^{1/2} b t_r^{3/2}} \exp\left[-\frac{(x - a t_r)^2}{2b^2 t_r}\right] \quad (5)$$

444 where x is the distance along the channel from the location where the impulse is input to
 445 the channel, t_r is time since the impulse was input into the channel, and the drift velocity
 446 a ($m s^{-1}$) and diffusion coefficient b^2 ($m^2 s^{-1}$) are defined as

$$447 \quad a = (1 + a_0)V \quad (6)$$

$$448 \quad b^2 = \frac{V^3}{g S F^2} (1 - a_0^2 F^2) \quad (7)$$

449 where F is the Froude number, g is the acceleration due to gravity ($m s^{-2}$), and a_0 is a
 450 constant equal to 2/3 when using Manning's equation (Troch et al., 1994). The large
 451 floods modeled in this study are assumed to have critical-flow conditions and therefore
 452 the Froude number is set to a constant value of 1.

453 The unit response discharge, q_{fd} ($m^2 s^{-1}$), at the outlet of a drainage basin can be
 454 computed from equations (3)-(5) by integrating the product of the cell response function
 455 $q_d(x,t)$ corresponding to a delta-function input of the normalized area function, $A(x)$, i.e.
 456 the spatial distribution of rainfall input. The integral is given by

457
$$q_{fd}(t_r) = \int_0^{t_p} \frac{Q_p}{w} dt' \int_0^L q_d(x, t_r - t') A(x) dx \quad (8)$$

458 where t_p is the time interval of measurement over which the unit impulse input (i.e. Q_p) is
 459 applied to the idealized square drainage basin, and t_r is the time after the input of the unit
 460 impulse that is long enough to capture the waxing and waning portions and the flood peak
 461 of the flood wave. The final peak discharge value, or Q_{fd} ($m^3 s^{-1}$), was calculated by
 462 multiplying the unit discharge q_{fd} ($m^2 s^{-1}$) by the channel width found through the formula
 463 derived from CRB data in Figure 4, and then selecting the largest value from the resulting
 464 hydrograph.

465

466 **3.7 Estimation of Uncertainty**

467 Confidence intervals (i.e. uncertainty estimates) were calculated to quantify the
 468 uncertainty in calculated rainfall intensities and associated Q_p and Q_{fd} values. In this
 469 study we estimated confidence intervals using a non-parametric method similar to that
 470 used to calculate quantiles for flow-duration curves (Parzen, 1979; Vogel and Fennessey,
 471 1994). Like quantile calculations, which identify a subset of the ranked data in the
 472 vicinity of each data point to estimate expected values and associated uncertainties, we
 473 estimated confidence intervals for our predictions based on the difference in Q_p values
 474 between each point and the next largest value in the ranked list. This approach quantifies
 475 the variation in the rainfall intensity value for a given contributing area and recurrence
 476 interval. In some cases the calculated uncertainties for rainfall intensities and associated
 477 Q_p and Q_{fd} values are infinite due to the values being past the frequency-magnitude
 478 distribution, i.e. there are not enough samples for these values to be determined and there
 479 are no finite numbers to sample. These values are not used in this study.

480 The resulting confidence intervals of rainfall intensity were used to calculate
 481 confidence intervals for Q_p and Q_{fd} . Confidence intervals for Q_p values were equal to the
 482 confidence intervals for rainfall intensity propagated through the calculation of Q_p (i.e.
 483 multiplying by contributing area). Confidence intervals for Q_{fd} values were calculated to
 484 be the same proportion of the Q_{fd} value as that set by the rainfall intensity value and its
 485 confidence intervals. For example, if the upper confidence interval was 120% of a
 486 rainfall-intensity value, the upper confidence interval for the Q_{fd} value associated with the

487 rainfall-intensity value is assumed to be 120% of the Q_{fd} value. This approach to
488 propagation of uncertainty treats all other variables in the calculations as constants and
489 additional uncertainty related to regression analyses on variables used in the flow-routing
490 algorithm such as slope, channel width, and runoff coefficients was not included.

491

492 **3.8 Testing the Effects of Climate Variability**

493 To quantify the robustness of our results with respect to climate variability, we
494 separated the NEXRAD data into El Niño and La Niña months using the multivariate
495 ENSO index (MEI). All months of data with negative MEI values (La Niña conditions)
496 were run together to calculate the rainfall intensity and Q_p values for contributing areas of
497 16, 256, and 4096 km², time intervals of 1 to 64 hours, and for 10-, 50-, 100-, and 500-
498 year recurrence intervals. This was repeated with all months of data with positive MEI
499 values (El Niño conditions). Figure 5 shows the distribution of negative and positive MEI
500 values during the 1996 to 2004 water years used in this study.

501

502 **4. Results**

503 **4.1 Channel Characteristics and Runoff Coefficients**

504 Least-squares regression of channel slopes and channel widths from the CRB
505 versus contributing area was used to estimate channel slope, channel width, and runoff
506 coefficients for each idealized basin of a specific contributing-area class. Channel slope
507 decreases as a power-law function of contributing area with an exponent of -0.30 ($R^2 =$
508 0.39), whereas channel width increases as a power-law function of contributing area with
509 an exponent of 0.28 ($R^2 = 0.65$; Fig. 4). These results follow the expected relationships
510 among channel slopes, widths, and contributing area, i.e. as contributing area increases
511 the channel slope decreases and the channel width increases.

512 Runoff coefficients for wet, medium, and dry antecedent-moisture conditions all
513 decrease with increasing contributing area following a logarithmic function, with the
514 slope of the line decreasing from wet to dry conditions. The fitness of the line to the data
515 also decreases for the wet to dry conditions, with the R^2 values for wet, medium, and dry
516 conditions equal to 0.78, 0.45, and 0.04, respectively. Runoff coefficients decrease with
517 increasing contributing area due to the increased probability of water loses as basin area

518 increases. Also, as expected, runoff coefficients are highest in basins with wet initial
519 conditions that are primed to limit infiltration and evapotranspiration.

520

521 4.2 Trends in Rainfall Intensity

522 Maximum rainfall intensities (i.e. the maximum among all time-interval-of-
523 measurement classes) for each contributing-area class and recurrence interval decrease
524 systematically as power-law functions of increasing contributing area for all recurrence
525 intervals with an average exponent of -0.18 ± 0.06 (error is the standard deviation of all
526 calculated exponents found from a weighed least-squares regression; average coefficient
527 of determination $R^2 = 0.78$). Note that maximum-rainfall-intensity results are not
528 presented because they are closely related to the plots of Q_p versus contributing area in
529 Figure 6, i.e. Q_p is simply the rainfall intensity multiplied by the contributing area. The
530 decrease in maximum rainfall intensity with contributing area can be seen in Table 1,
531 where maximum rainfall intensities over contributing areas of $11,664 \text{ km}^2$ are 45% to 8%
532 of maximum rainfall intensity values for basin areas of 16 km^2 in both the UCRB and
533 LCRB (Table 1). The largest decrease in maximum rainfall intensity values between the
534 smallest and largest contributing areas were found for the largest recurrence interval (e.g.
535 500-year) for both the UCRB and LCRB. The decrease in maximum rainfall intensity
536 with increasing contributing area suggests that there is a spatial limitation to storms of a
537 given rainfall intensity.

538 Differences among maximum rainfall intensities for the four recurrence intervals
539 as a function of contributing area are larger in the UCRB than in the LCRB (Table 1).
540 This larger “spread” in the maximum rainfall intensities in the UCRB relative to the
541 LCRB is also propagated throughout the maximum rainfall and flood discharge
542 calculations. For both the UCRB and LCRB, the difference between the 50- and 100-year
543 recurrence interval values was the smallest (Table 1). These trends show that maximum
544 rainfall intensities vary much more as a function of recurrence interval in the UCRB
545 compared with the LCRB.

546 Maximum rainfall intensities associated with a 10-year recurrence interval are
547 similar in the LCRB and UCRB, while intensities were higher in the UCRB than the
548 LCRB for recurrence intervals of 50-, 100-, and 500-years (Table 1). The results of the

549 comparison between the two basins suggest that common (i.e. low-recurrence-interval)
550 rainfall events will have similar maximum rainfall intensities in the UCRB and LCRB,
551 but that rare (i.e. high-recurrence-interval) rainfall events will have higher maximum
552 rainfall intensities in the UCRB than in the LCRB for the same recurrence interval.

553 Maximum precipitation intensities associated with the four defined recurrence
554 intervals are similar to previously published values. In general the values we calculate for
555 the LCRB and the UCRB for the 10-, 50-, and 100-year recurrence intervals are on the
556 order of 10s of mm h^{-1} . This is similar to the spread in values reported on precipitation
557 intensity maps for the same duration and recurrence interval in Hershfield (1961).

558 However, the values reported by Hershfield (1961) are slightly higher (by less than 20
559 mm h^{-1}) in the LCRB for the three recurrence intervals and in the UCRB for the 10-year
560 recurrence interval than values calculated in this study. The values calculated here are
561 also broadly consistent with presented precipitation frequency estimates for points within
562 the LCRB and UCRB provided by the NOAA Atlas 14 Point Precipitation Frequency
563 Estimates website (http://hdsc.nws.noaa.gov/hdsc/pfds/pfds_map_cont.html). Due to the
564 difference in how precipitation intensities are measured and how the frequencies are
565 calculated the values are expected to be slightly different but within the same order of
566 magnitude.

567

568

569 **4.3 Trends in Q_p**

570 Maximum precipitation (here only rainfall) discharges (Q_p hereafter) increase
571 with contributing area as power-law functions with an average exponent of 0.82 ± 0.06
572 (error is the standard deviation of all calculated exponents) based on weighed least-
573 squares regressions on the data ($R^2 = 0.98$) for all recurrence intervals and for both the
574 UCRB and LCRB (Fig. 6). These Q_p values for a given contributing-area class and
575 recurrence interval are the largest values taken from the multiple values calculated for
576 each of the seven time intervals of measurement as explained in Section 3.3. By taking
577 the maximum values, the resulting Q_p FMACs approximate the upper envelope of values
578 of a given recurrence interval. In this study the FMAC follows a power-law function that
579 shows that Q_p increases predictably across the range in contributing areas. As with the

580 maximum rainfall intensity results, differences between Q_p values of different recurrence
581 intervals for a given contributing area were larger for the UCRB than the LCRB (Fig. 6).

582 In general, confidence intervals for Q_p values increase with increasing
583 contributing-area class (Table 1 and Fig. 6). The large values of the highest contributing-
584 area classes and highest recurrence intervals show the spatial limitation of the method,
585 meaning that at these contributing-area classes and recurrence intervals the values are
586 sampled from the largest ranked value and have infinite confidence intervals. These
587 values include the 50-, 100-, and 500-year recurrence intervals for the UCRB and the
588 100- and 500-year recurrence intervals for the LCRB at the 11,664 km² contributing-area
589 class. These values also include the 100- and 500-year recurrence intervals for the UCRB
590 and the 500-year recurrence intervals for the LCRB at the 4,096 km² contributing-area
591 class. Values with infinite confidence intervals are not included in Fig. 6 due to their high
592 uncertainties.

593

594 4.4 Trends in Q_{fd}

595 Maximum Q_{fd} values (hereafter Q_{fd}), i.e. the largest values taken for the multiple
596 values calculated for each time interval of measurement for a given contributing-area
597 class and recurrence interval, were used to plot FMACs for wet, medium, and dry
598 conditions for both the UCRB and LCRB (Fig. 7). In general, FMACs for Q_{fd} values
599 follow the power-law relationship shown in the Q_p FMACs until contributing areas of
600 ~1,000 km², where the curves begin to very slightly flatten or decrease. As with the Q_p
601 values, Q_{fd} values representing some of the higher recurrence intervals converge to the
602 same value (i.e. the value corresponding to the highest rainfall intensity for the
603 contributing-area class) at contributing areas of \approx 10,000 km² the and the confidence
604 intervals become infinite (Table 2). This convergence of Q_{fd} values at the largest
605 contributing areas is due to the reduction in the range of values and the number of
606 samples from which to calculate the associated values for each recurrence interval.

607 In general, The UCRB Q_{fd} FMACs (Fig. 7A, C, and E) are slightly higher in
608 magnitude and span a larger range of magnitudes than the FMACs for the LCRB. For
609 both basins, FMACs for the wet, medium, and dry conditions resulting in the highest,

610 middle, and lowest magnitudes, respectively. This trend is expected due to the lowering
611 of runoff coefficients and available water as conditions become drier.

612 FMACs of Q_{fd} for the LCRB plot below published FECs for the LCRB and U.S.
613 (Fig. 7B, D, F) at low contributing areas, but meet and/or exceed the LCRB FEC for
614 contributing areas above $\approx 1,000 \text{ km}^2$ and $\approx 100 \text{ km}^2$ for dry and wet antecedent-moisture
615 conditions, respectively. The FMACs for the LCRB do not exceed the U.S. FEC. All of
616 the FMACs of Q_{fd} for the UCRB exceed the LCRB FEC for wet conditions, with the
617 FMACs of lower recurrence intervals exceeding the curve at higher contributing areas
618 than the FMACs of higher recurrence intervals (Fig. 7A). The 500-year FMAC for wet
619 conditions approximate the U.S. FEC for contributing areas between ≈ 100 to $1,000 \text{ km}^2$.
620 These results suggests that under certain antecedent-moisture conditions, and in basins of
621 certain contributing areas, the LCRB produces floods that exceed the maximum recorded
622 floods in the LCRB and the UCRB produces floods of magnitudes on par with the
623 maximum recorded floods in the U.S.

624

625 **4.5 The Effects of ENSO on Rainfall**

626 Definitive differences in maximum rainfall intensities and Q_p values were found
627 between months with positive versus months with negative MEI values (Table 3). For
628 very small contributing areas (16 km^2) in the LCRB maximum rainfall intensities and Q_p
629 values are similar during negative and positive MEI conditions. Larger contributing areas
630 (256 and $4,096 \text{ km}^2$) show higher maximum rainfall intensities during negative MEI
631 conditions regardless of recurrence interval. Values of Q_p show the same trend as the
632 maximum rainfall intensity in the LCRB. In the UCRB, maximum rainfall intensities and
633 Q_p values during negative MEI conditions are higher than those during positive MEI
634 conditions regardless of recurrence interval.

635

636 **5. Discussion**

637 **5.1 Use and Accuracy of NEXRAD Products**

638 NEXRAD products are widely used as precipitation inputs in rainfall-runoff
639 modeling studies due to the spatially complete nature of the data necessary for hydrologic
640 and atmospheric models (Ogden and Julien, 1994; Giannoni et al., 2003; Kang and

641 Merwade, 2011). In contrast to past studies similar in scope to this study (Castellarin et
642 al., 2005; Castellarin, 2007; Castellarin et al., 2009) we did not use rain-gauge data and
643 only used NEXRAD products to determine the FMACs for precipitation and flood
644 discharges. We favor NEXRAD products due to the spatial completeness of the data.

645 Intuitively, NEXRAD products that are spatially complete and that average
646 precipitation over a 4 km by 4 km area would not be expected to match rain-gauge data
647 within that area precisely (due to the multi-scale variability of rainfall), although some
648 studies have tried to address this discrepancy (Sivapalan and Bloschl, 1998; Johnson et
649 al., 1999). Xie et al. (2006) studied a semi-arid region in central New Mexico and found
650 that hourly NEXRAD products overestimated the mean precipitation relative to rain-
651 gauge data in both monsoon and non-monsoon seasons by upwards of 33% and 55%,
652 respectively. Overestimation of precipitation has also been noted due to the range and the
653 tilt angle at which radar reflectivity data are collected (Smith et al., 1996).
654 Underestimation of precipitation by NEXRAD products relative to rain gauge data has
655 also been observed (Smith et al., 1996; Johnson et al., 1999), however.

656 Under- and over-estimation of precipitation by NEXRAD products in relation to
657 rain-gauge data is partly due to the difference in sampling between areal NEXRAD
658 products and point data from rain gauges and partly due to sampling errors inherent to
659 both methods. For example, NEXRAD products include problems such as the use of
660 incorrect Z-R relationships for high intensity storms and different types of precipitation,
661 such as snow and hail (Baeck and Smith, 1998). Also, because of its low reflectivity,
662 snow in the NEXRAD products is measured as if it were light rain (David Kitzmiller,
663 personal communication, January 10, 2012). This means the NEXRAD products likely
664 underestimate snowfall and therefore snowfall is not fully accounted for in this study.
665 Due to snowfall not being included in this study, associated snowpack and snowmelt
666 effects were also not accounted for. Rain gauges can also suffer from a number of
667 measurement errors that usually result in an underestimation of rainfall (Burton and Pitt,
668 2001). In addition, gridded rainfall data derived from rain gauges are not spatially
669 complete and therefore must be interpolated between point measurements to form a
670 spatially complete model of rainfall. It is impossible to discern which product is more
671 correct due to the differences in measurement techniques and errors, but by taking both

672 products and combining them into one, the Stage III NEXRAD precipitation products
673 generate the best precipitation estimate possible for this study. Moreover, it should be
674 noted that 100-year flood magnitude predictions based on regression equations have very
675 large relative error bars (ranging between 37 to 120% in the western U.S.; Parrett and
676 Johnson, 2003) and that measurements of past extreme floods can have significant errors
677 ranging from 25% to 130% depending on the method used (Baker, 1987). As such, even a
678 ~50% bias in NEXRAD-product-derived precipitation estimates is on par or smaller than
679 the uncertainty associated with an analysis of extreme flood events.

680 As stated previously, the NEXRAD precipitation estimates used here do not
681 include snowfall and other non-rainfall precipitation types. In this study we also do not
682 include snowpack information into our flood discharge calculations. The omission of
683 snowpack is a reasonable assumption for our low elevation, warm regions within most of
684 the UCRB and LCRB. However, we acknowledge some of our higher elevation areas at
685 higher latitudes may be underestimating the maximum flood discharge by only including
686 rainfall-derived runoff. If the methodology in this paper were applied to a snowmelt-
687 dominated region, snowpack would need to be added to accurately estimate the
688 maximum flood discharge.

689

690 **5.2 Comparison of FMACs to Published FECs**

691 FMACs of Q_{fd} exhibit a similar shape and similar overall range in magnitudes as
692 previously published FECs, derived from stream-gauge and paleoflood records, for the
693 LCRB and U.S. (Fig. 7). In general, the FMACs exceed or match published FECs at
694 larger contributing areas, and are lower than or on par with published FECs at the
695 smallest contributing areas (Fig. 7).

696 All FMACs except the 500-year recurrence-interval curve for the UCRB under
697 wet conditions are positioned well below the U.S. FEC presented by Costa (1987; Fig.
698 7A). The similarity between the 500-year recurrence interval Q_{fd} FMAC for the UCRB
699 under wet conditions and the U.S. FEC suggests that the U.S. FEC includes floods of
700 larger recurrence-intervals, which are similar in magnitude to the 500-year recurrence-
701 interval floods within the UCRB. The approximation of the U.S. FEC by the 500-year
702 UCRB FMAC is a significant finding due to the fact that the U.S. FEC includes storms

703 from other regions of the U.S. with extreme climatic forcings (i.e. hurricanes, extreme
704 convection storms, etc.).

705 The Q_{fd} FMACs for the LCRB can be directly compared to the FEC for the LCRB
706 presented by Enzel et al. (1993). At contributing areas smaller than approximately 100
707 km^2 , Q_{fd} FMACs for wet conditions and all recurrence intervals are positioned below the
708 LCRB FEC, but at larger contributing areas Q_{fd} FMACs exceed or approximate the
709 LCRB FEC. Q_{fd} FMACs calculated for medium and dry antecedent conditions show the
710 same trend, but exceed the LCRB FEC at a larger contributing areas ($\geq 1,000 \text{ km}^2$). This
711 comparison suggests that although the FMACs overlap the overall range of flood
712 magnitudes of the LCRB FEC, the two methods are not capturing the same trend for
713 extreme flood discharges and the LCRB is capable of producing floods larger than those
714 on record.

715 The difference in the slope of the FMACs, and specifically the exceedance of the
716 published LCRB FEC, suggests that the two methods are not capturing the same
717 information. This difference may be due to the difference in how the data are sourced for
718 each method. FECs are created as regional estimates of maximum flood discharges and
719 are based on stream-gauging station and paleoflood data. The FECs are then used to
720 provide flood information for the region, including ungauged and unstudied drainage
721 basins. FECs are limited to the number of stream gauges employed by public and private
722 parties and do not include all basins within a region. In general, FECs may underestimate
723 maximum floods in larger basins, relative to smaller basins, because there are a larger
724 number of smaller basins to sample than larger basins. This sample-size problem
725 introduces bias in the record where flood estimates for smaller contributing areas may be
726 more correct than estimates for larger basins. In this study, the regional precipitation
727 information given by the NEXRAD network is used to form the FMAC, therefore taking
728 advantage of the entire region and using precipitation data to calculate flood discharges,
729 rather than directly measuring flood discharges. This sampling scheme allows for much
730 larger sample sizes for the range of contributing areas, therefore minimizing the sample
731 bias of the traditional FEC.

732 This study aimed to introduce the new method of the FMAC and therefore
733 improve upon the traditional methods of the FEC. By calculating FMACs we provide

frequency and magnitude information of possible flood events for a given region in contrast to the FECs that only provide an estimate of the largest flood on record. This information is vital for planning and infrastructure decisions and the accurate representation of precipitation and flooding in design-storm and watershed modeling. In addition, the fact that the FMACs match the FECs for large (500-year) recurrence intervals and do not exhibit the same trends suggests that the FMACs are capturing different samples than the FECs. This indicates that by using the NEXRAD products, the FMACs may provide a more inclusive flood dataset for a region (especially ungauged areas) than the traditional stream-gauge records.

743

744 **5.3 Precipitation Controls on the Form of the FEC**

745 Q_p FMACs were shown to have a strong (average $R^2 = 0.93$) power-law relationship between Q_p and contributing area for all recurrence intervals. Figure 8 shows 746 a conceptualized FEC where the concave-down shape is created when the observed 747 envelope curve diverges from the constant positive power-law relationship between Q_p 748 and contributing area. This diversion creates a “gap” between the two curves and 749 indicates that flood discharge is not a simple power-law function of contributing area. 750 Three mechanisms have been proposed to explain the “gap” and characteristic concave- 751 down shape of FECs: (1) integrated precipitation (i.e. total precipitation over an area) is 752 more limited over larger contributing areas compared to smaller contributing areas 753 (Costa, 1987), (2) a relative decrease in maximum flood discharges in larger contributing 754 areas due to geomorphic dispersion (Rodriguez-Iturbe and Valdes, 1979, Rinaldo et al., 755 1991, Saco and Kumar, 2004), and (3) a relative decrease in maximum flood discharges 756 in larger basins due to hydrodynamic dispersion (Rinaldo et al., 1991). The first 757 explanation, proposed by Costa (1987), suggests that there is a limitation to the size of a 758 storm and the amount of water that a storm can precipitate. The effect of precipitation 759 limitations may be evidenced by the decreasing maximum rainfall intensities with 760 increasing contributing area. However, the strong power-law relationship between Q_p and 761 contributing area for all recurrence intervals indicates that Q_p is, in general, increasing 762 predictably over the range of contributing areas used in this study. Even if precipitation 763 limitations affect the shape of the curve, this single hypothesis does not account for all of 764

765 the concave-down shape of each FEC suggesting that other mechanisms are important to
766 creating the characteristic shape. However, it is important to note that the importance of
767 each mechanism may be different for different locations.

768

769 **5.4 Climate Variability in the NEXRAD Data**

770 The results from comparing negative and positive MEI conditions in the UCRB
771 and LCRB are generally consistent with ideas about ENSO and how it affects
772 precipitation in the western U.S. In the LCRB, during negative MEI conditions, small,
773 frequent storms have similar or slightly higher maximum rainfall intensities and Q_p
774 values than during positive MEI conditions. This similarity between the two conditions
775 may be explained by the balancing of increased winter moisture during El Niño in the
776 southwestern U.S. (Hidalgo and Dracup, 2003) and increased summer moisture through
777 the strengthening of the NAM system and the convective storms it produces during La
778 Niña conditions (Castro et al., 2001; Grantz et al., 2007). In general, the strengthening of
779 the NAM may explain the higher maximum rainfall intensities and Q_p values during
780 negative MEI conditions in the LCRB. Strengthening of the NAM may be due in part to
781 the large temperature difference between the cool sea surface of the eastern Pacific Ocean
782 and the hot land surface of the southwestern U.S. and northwestern Mexico during La
783 Niña conditions. The large temperature gradient increases winds inland, bringing the
784 moisture associated with the NAM (Grantz et al., 2007). In the UCRB it is during
785 negative MEI conditions, where the highest maximum rainfall intensities and Q_p values
786 for all recurrence intervals occur. This suggests that the UCRB is affected by ENSO
787 much like the northwestern U.S., where wetter winters are affiliated with La Niña and not
788 El Niño conditions (Cayan et al., 1999; Hidalgo and Dracup, 2003). It is important to
789 note that this comparison is of intensity rates and not total precipitated moisture so the
790 MEI condition resulting in wetter conditions is not known.

791 In addition to the ENSO analysis, by investigating previous studies we see that,
792 along with natural yearly precipitation variability, the 1996 to 2004 water years included
793 many atmospheric river events (Dettinger, 2004; Dettinger et al., 2011). It is important
794 that these events were included due to their ability to greatly increase winter precipitation
795 in the UCRB and LCRB (Rutz and Steenburgh, 2012). Atmospheric river events

796 (sometimes known as Pineapple Express events) can also be tied to major Pacific climate
797 modes such as the ENSO (Dettinger, 2004; Dettinger, 2011), the Pacific Decadal
798 Oscillation (PDO; Dettinger, 2004), and the North Pacific Gyre Oscillation (NPGO;
799 Reheis et al., 2012) in southern California. Unfortunately, correlations between
800 atmospheric river events are unknown and/or less clear for the interior western U.S.
801 However, all three of these Pacific climate modes shifted during the 9-year study period
802 in ~1998 to 1999 (Reheis et al., 2012) indicating that both positive and negative
803 conditions of the ENSO, PDO, and NPGO exist in the NEXRAD products used in this
804 study.

805 The presence of distinct trends in maximum rainfall-intensity and Q_p values
806 calculated for negative and positive MEI conditions, as well as the information in the
807 literature on atmospheric river events, indicates the NEXRAD products used in this study
808 incorporate circulation-scale weather patterns. In addition, the patterns in maximum
809 rainfall intensities and Q_p values during different MEI conditions agree with common
810 understanding of the effects of ENSO on the western U.S. and provide evidence that the
811 data and methods used in this paper to analyze precipitation are reliable. This analysis
812 shows that the NEXRAD products worked well in this location and that using radar-
813 derived precipitation products may be useful for identifying precipitation and climatic
814 trends in other locations where the FMAC method can be applied.

815

816 **6. Conclusions**

817 In this study we present the new FMAC method of calculating precipitation and
818 flood discharges of a range of recurrence intervals using radar-derived precipitation
819 estimates combined with a flow-routing algorithm. This method improves on the
820 traditional FEC by assigning recurrence interval information to each value and/or curve.
821 Also, instead of relying on stream-gauge records of discharge, this method uses up-to-
822 date and spatially complete radar-derived precipitation estimates (in this case NEXRAD
823 products) to calculate flood discharges using flow-routing algorithms. This study presents
824 an alternative data source and method for flood-frequency analysis by calculating
825 extreme (high recurrence interval) event magnitudes from a large sample set of
826 magnitudes made possible by sampling the radar-derived precipitation estimates.

827 The FMACs for Q_p and Q_{fd} for the UCRB were similar to those produced for the
828 LCRB. In general, all recurrence-interval curves followed the same general trend,
829 indicating that the mechanisms of precipitation and flood discharge are similar for the
830 two basins. However, there were some differences between the two basins. Overall, there
831 were larger differences between curves of different recurrence intervals for the UCRB
832 than the LCRB suggesting a larger range in maximum rainfall intensities, and therefore
833 Q_p and Q_{fd} , in the UCRB relative to the LCRB. For both the UCRB and LCRB the 50-
834 and 100-year recurrence interval curves for all precipitation and discharge FMACs were
835 the most similar. This similarity may mean that although historical discharge records are
836 short, having a 50-year record may not underestimate the 100-year flood as much as one
837 might expect. Also, for Q_p and Q_{fd} , low recurrence-interval values were slightly higher in
838 the LCRB than in the UCRB. This relationship was opposite for high recurrence-interval
839 values. This likely points to a general hydroclimatic difference between the two basins,
840 with the LCRB receiving high intensity storms annually due to the NAM and the UCRB
841 receiving more intense and rarer winter frontal storms.

842 Power-law relationships between maximum rainfall intensity, Q_p , and
843 contributing area were also found in this study. Maximum rainfall intensities decreased as
844 a power-law function of contributing area with an average exponent of -0.18 ± 0.06 for
845 all recurrence intervals. Q_p values for all recurrence intervals increased as a power-law
846 function of contributing area with an exponent of approximately 0.82 ± 0.06 on average.
847 Based on the constant power-law relationship between Q_p and contributing area, the
848 “gap” or characteristic concave-down shape of published FEC are likely not caused by
849 precipitation limitations.

850 In general, the FMACs of Q_{fd} calculated in this study are lower than, and exceed,
851 the published FECs for the LCRB at lower and higher contributing areas. All FMACs of
852 Q_{fd} were positioned well below the U.S. FEC except the UCRB 500-year FMAC, which
853 approximated the U.S. FEC during wet antecedent-moisture conditions. All FMACs of
854 Q_{fd} for all moisture conditions in the LCRB closely approximated the same magnitudes
855 as the published LCRB FEC, but exceeded it for larger contributing areas. The higher
856 estimates of flood discharges at larger contributing areas may be the result of the

857 difference of sampling methods and are likely not erroneous and may be proved true by
858 future events.

859 Lastly, the approximately 9 years of NEXRAD products were found to be a good
860 representation of climate in the CRB. This conclusion was made based on differences in
861 precipitation between positive and negative ENSO conditions in both the UCRB and
862 LCRB and additional data found in the literature. In general, the UCRB was found to
863 have a hydroclimatic regime much like that of the northwestern U.S. where El Niño
864 conditions result in lower maximum rainfall intensities and amounts and La Niña
865 conditions result in higher maximum rainfall intensities. The LCRB showed a more
866 complex trend with similar maximum rainfall intensities for both El Niño and La Niña
867 conditions.

868 Here this method is applied to the UCRB and LCRB in the southwestern U.S., but
869 could be applied to other regions of the U.S. and the world with variable climate and
870 storm types where radar-derived precipitation estimates are available. In this study we
871 used set values for contributing area, drainage basin shape, time intervals of
872 measurement, and recurrence intervals that can be changed based on the focus of future
873 studies. However, it is also important to note that a number of assumptions were made in
874 this study that simplified our analysis, most importantly: (1) space for time substitution,
875 or regionalization, was used to increase the number of samples and assumed that
876 observations were independent and sampled from the same distribution; (2) it was
877 assumed that the time period length and the spatial and temporal sampling scales were
878 sufficient to create a representative sample from the observations; (3) it was assumed that
879 similar flood-generating and flow-routing mechanisms (and related variables such as
880 runoff coefficients) were present in each basin regardless of size or location. These
881 assumptions allowed us to form and apply the methods described here to our study area
882 but may not apply to all areas. Other variables such as snowpack, elevation, land use, and
883 climate change that were not included in this study should be explored in conjunction
884 with this methodology to better understand controls on precipitation and flooding. The
885 absence of these elements from the method here may limit the application of this method
886 to other locations.

887

888 **Acknowledgments**

889 This study was supported by the Jemez River Basin and Santa Catalina Critical
890 Zone Observatory NSF grants EAR-0724958 and EAR-1331408. We would like to thank
891 Vic Baker, Phil Pearthree, Peter Troch, and Katie Hirschboeck for helpful discussions
892 and suggestions.

893 **References**

894 Baeck, M.L. and Smith, J.A.: Rainfall estimates by the WSR-88D for heavy rainfall
895 events, *Weather Forecast.*, 13, 416-436, 1998.

896

897 Baker, V.R.: Paleoflood hydrology and extraordinary flood events, *J. Hydrol.*, 96, 77-99,
898 1987.

899

900 Brutsaert, W.: Review of Green's functions for linear open channels, *J. Eng. Mech.-*
901 *ASCE*, 99, 1247-1257, 1973.

902

903 Buishand, T.A.: Extreme rainfall estimation by combining data from several sites,
904 *Hydrologic. Sci. J.*, 36, 4, doi:10.1080/02626669109492519, 1991.

905

906 Burton, G.A., Jr. and Pitt, R.E (Eds.): *Stormwater effects handbook: a toolbox for*
907 *watershed managers, scientists, and engineers*, Lewis Publishers, Boca Raton, Florida,
908 2001.

909

910 Cañon, J., González, J., and Valdes, J.: Precipitation in the Colorado River Basin and its
911 low frequency associations with PDO and ENSO signals, *J. Hydrol.*, 333, 252-264, 2007.

912

913 Castellarin, A.: Probabilistic envelope curves for design flood estimation at ungauged
914 sites, *Water Resour. Res.*, 43, W04406, doi:10.1029/2005WR004384, 2007.

915

916 Castellarin, A., Vogel, R.M., and Matalas, N.C.: Probabilistic behavior of a regional
917 envelope curve, *Water Resour. Res.*, 41, W06018, doi:10.1029/2004WR003042, 2005.

918

919 Castellarin, A., Merz, R., and Bloschl, G.: Probabilistic envelope curves for extreme
920 rainfall events, *J. Hydrol.*, 378, 263-271, 2009.

921

922 Castro, C.L., McKee, T.B., and Pielke, R.A. Sr.: The relationship of the North American
923 Monsoon to Tropical and North Pacific surface temperatures as revealed by observational
924 analyses, *J. Climate*, 14, 4449-4473, 2001.

925

926 Cayan, D.R., Redmond, K.T., and Riddle, L.G.: ENSO and hydrologic extremes in the
927 western United States, *J. Climate*, 12, 2881-2893, 1999.

928

929 Costa, J.E.: A comparison of the largest rainfall-runoff floods in the United States with
930 those of the People's Republic of China and the World, *J. Hydrol.*, 96, 101-115, 1987.

931

932 Crippen, J.R. and Bue, C.D.: Maximum flood flows in the conterminous United States,
933 U.S. Geological Survey Water Supply Paper 1887, 1977.

934

935 Dalrymple, T.: Flood-frequency analyses, *Manual of Hydrology: Part 3*, U.S. Geological
936 Survey Water Supply Paper 1543, 80 p., 1960.

937

938 Dettinger, M.: Fifty-two years of "Pineapple-Express" storms across the west coast of
939 North America, U.S. Geological Survey, Scripps Institution of Oceanography for the
940 California Energy Commission, PIER Energy-Related Environmental Research, CEC-
941 500-2005-004, 2004.

942

943 Dettinger, M.D., Ralph, F.M., Das, T., Neiman, P.J., and Cayan, D.R.: Atmospheric
944 rivers, floods, and the water resources of California, *Water*, 3, 445-478, 2011.

945

946 Enzel, Y., Ely, L.L., House, P.K., Baker, V.R., and Webb, R.H.: Paleoflood evidence for
947 a natural upper bound to flood magnitudes in the Colorado River Basin, *Water Resour.*
948 *Res.*, 29, 2287-2297, 1993.

949

950 Etheredge, D., Gutzler, D.S., and Pazzaglia, F.J.: Geomorphic response to seasonal
951 variations in rainfall in the Southwest United States, *Geol. Soc. Am. Bull.*, 116, 606-618,
952 2004.

953

954 Federal Emergency Management Agency: Modernizing FEMA's flood hazard mapping

955 program: Recommendations for using future-conditions hydrology for the National Flood

956 Insurance Program, Final Report, U.S. Department of Homeland Security, 2001.

957

958 Fulton, R.A., Breidenbach, J.P., Seo, D.J., Miller, D.A., and O'Bannon, T.: The WSR-

959 88D algorithm, *Weather Forecast.*, 13, 377-395, 1998.

960

961 Giannoni, F., Smith, J.A., Zhang, Y., and Roth, G., 2003: Hydrologic modeling of

962 extreme floods using radar rainfall estimates, *Adv. Water Resour.*, 26, 195-203, 2003.

963

964 Grantz, K., Rajagopalan, B., Clark, M., and Zagona, E.: Seasonal shifts in the North

965 American Monsoon, *J. Climate*, 20, 1923-1935, 2007.

966

967 Henderson, F.M.: Some properties of the unit hydrograph, *J. Geophys. Res.*, 68, 4785-

968 4793, 1963.

969

970 Herschy, R.: The world's maximum observed floods, *Flow Meas. Instrum.*, 13, 231-235,

971 2002.

972

973 Hidalgo, H.G. and Dracup, J.A.: ENSO and PDO Effects on hydroclimatic variations of

974 the Upper Colorado River Basin, *J. Hydrometeorol.*, 4, 5-23, 2003.

975

976 Hershfield, D.M.: Rainfall Frequency Atlast of the United States for Durations from 30

977 minutes to 24 hours and periods from 1 to 100 years, U.S. Weather Bureau Technical

978 Paper No. 40, 65 p., 1961.

979

980 Hosking, J.R.M., and Wallis, J.R.: The effect of intersite dependence on regional flood

981 frequency analysis. *Water Resour. Res.*, 24, 588-600, 1988.

982

983 Hosking, J.R.M., and Wallis, J.R.: Regional Frequency Analysis, Cambridge University
984 Press, New York, 283 p., 2005.

985

986 House, P.K. and Hirschboeck, K.K.: Hydroclimatological and paleohydrological context
987 of extreme winter flooding in Arizona, 1993, in: Larson, R.A. and Slosson, J.E. (Eds.),
988 Storm-Induced Geologic Hazards: Case Histories from the 1992-1993 Winter in Southern
989 California and Arizona, Geological Society of America Reviews in Engineering Geology,
990 vol. XI, Boulder, Colorado, 1-24, 1997.

991

992 Johnson, D., Smith, M., Koren, V., and Finnerty, B.: Comparing mean areal precipitation
993 estimates from NEXRAD and rain gauge networks, *J. Hydrol. Eng.*, 4, 117-124, 1999.

994

995 Kang, K. and Merwade, V.: Development and application of a storage-release based
996 distributed hydrologic model using GIS, *J. Hydrol.*, 403, 1-13, 2011.

997

998 Li, Bai: Current status of weather radar data exchange, World Meteorological
999 Organization Workshop on Radar Data Exchange, Exeter, UK, April 2013, 16.IV.2013,
1000 2013.

1001

1002 Marani, M., Rinaldo, A., Rigon, R., Rodriguez-Iturbe, I.: Geomorphological width
1003 functions and the random cascade, *Geophys. Res. Lett.*, 21, 2123-2126, 1994.

1004

1005 Mesa, O.J. and Mifflin, E.R.: On the relative role of hillslope and network geometry in
1006 hydrologic response, in: Gupta, V.K., Rodriguez-Iturbe, I., and Wood, E.F., (Eds.), *Scale*
1007 *Problems in Hydrology*, D. Reidel, Dordrecht, Netherlands, 1-17, 1986.

1008

1009 Miller, A.J.: Flood hydrology and geomorphic effectiveness in the central Appalachians,
1010 *Earth Surf. Processes*, 15, 119-134, 1990.

1011

1012 Milly, P.C.D., Betancourt, J., Falkenmark, M., Hirsch, R.M., Kundzewicz, Z.W.,
1013 Lettenmaier, D.P., and Stouffer, R.J.: Stationarity is dead: Whither water management?,
1014 Science, 319, 573-574, 2008.

1015

1016 Moody, T., Wirtanen, M., Yard, S.N.: Regional relationships for bankfull stage in natural
1017 channels of the arid southwest, National Channel Design Inc., Flagstaff, AZ, 38 pp.,
1018 2003.

1019

1020 Morrison, J.E. and Smith, J.A.: Stochastic modeling of flood peaks using the generalized
1021 extreme value distribution, Water Resour. Res., 38(12), 1305
1022 doi:10.1029/2001WR000502, 2002.

1023

1024 Moussa, R.: What controls the width function shape, and can it be used for channel
1025 network comparison and regionalization?, Water Resour. Res., 44, W08456,
1026 doi:10.1029/2007WR006118, 2008.

1027

1028 National Atlas: <http://www.nationalatlas.gov/atlasftp.html#hucs00m>, last access: 8
1029 August 2014

1030

1031 Niezgoda, S. and West, T. (2012) Relationships between Watershed and Stream
1032 Characteristics and Channel Forming Discharge in Snowmelt Dominated Streams. World
1033 Environmental and Water Resources Congress 2012: pp. 1575-1584.
1034 doi: 10.1061/9780784412312.157

1035

1036 NOAA HDSG: http://dipper.nws.noaa.gov/hdsb/data/nexrad/cbrfc_stageiii.php, last
1037 access: 8 August 2014.

1038

1039 NOAA Atlas 14 Point Precipitation Frequency Estimates:
1040 http://hdsc.nws.noaa.gov/hdsc/pfds/pfds_map_cont.html, last access: 8, June 2016.

1041

1042 Ogden, F.L. and Julien, P.Y.: Runoff model sensitivity to radar rainfall resolution, *J.
1043 Hydrol.*, 158, 1-18, 1994.

1044

1045 Parrett, C. and Johnson, D.R.: Methods for estimating flood frequency in Montana based
1046 on data through water year 1998, U.S. Geological Survey Water-Resources Investigations
1047 Report 03-4308, 2003.

1048

1049 Parzen, E.: Nonparametric statistical data modeling, *J. Am. Statist. Assoc.*, 74, 365, 105-
1050 121, 1979.

1051

1052 Puente, C.E. and Sivakumar, B.: A deterministic width function model, *Nonlinear Proc.
1053 Geoph.*, 10, 525-529, 2004.

1054

1055 RadarEU: <http://www.radareu.cz/>, last access 1 August, 2014.

1056

1057 Reed, S.M. and Maidment, D.R.: Coordinate transformations for using NEXRAD data in
1058 GIS-based hydrologic modeling, *J. Hydrol. Eng.*, 4, 174-182, 2006.

1059

1060 Reheis, M.C., Bright, J., Lund, S.P., Miller, D.M., Skipp, G., and Fleck, R.J.: A half-
1061 million-year record of paleoclimate from the Lake Manix Core, Mojave Desert,
1062 California, *Palaeogeogr. Palaeocl.*, 365-366, 11-27, 2012.

1063

1064 Rinaldo, A., Marani, A., and Rigon, R.: Geomorphological dispersion, *Water Resour.
1065 Res.*, 27, 513-525, 1991.

1066

1067 Rinaldo, A., Vogel, G.K., Rigon, R., Rodriguez-Iturbe, I.: Can one gauge the shape of a
1068 basin?, *Water Resour. Res.*, 31, 1119-1127, 1995.

1069

1070 Rodriguez-Iturbe, I. and Valdes, J.B.: The geomorphic structure of hydrologic response,
1071 *Water Resour. Res.*, 15, 1409-1420, 1979.

1072

1073 Rosenburg, E.A., Clark, E.A., Steinemann, A.C., and Lettenmaier, D.P.: On the
1074 contribution of groundwater storage to interannual streamflow anomalies in the Colorado
1075 River basin, *Hydrol. Earth Sys. Sc.*, 17, 1475-1491, 2013.

1076

1077 Rutz, J.J. and Steenburgh, W.J.: Quantifying the role of atmospheric rivers in the interior
1078 western United States, *Atmos. Sci. Lett.*, 13, 257-261, doi:10.1002/asl.392, 2012.

1079

1080 Saco, P.M. and Kumar, P.: Kinematic dispersion effects of hillslope velocities, *Water
1081 Resour. Res.*, 40, W01301, doi:10.1029/2003WR002024, 2004.

1082

1083 Sankarasubramanian, A. and Vogel, R.M.: Hydroclimatology of the continental United
1084 States, *Geophys. Res. Lett.*, 30, 1363, doi:10.1029/2002GL015937, 2003.

1085

1086 Shedd, R.C. and Fulton, R.A.: WSR-88D precipitation processing and its use in National
1087 Weather Service hydrologic forecasting, in: *Proceedings, Engineering Hydrology:
1088 Proceedings of the Symposium Sponsored by the Hydrology Division of American
1089 Society of Civil Engineers*, 844-848, 1993.

1090

1091 Sivapalan, M. and Bloschl, G.: Transformation of point rainfall to areal rainfall:
1092 Intensity-duration-frequency curves, *J. Hydrol.*, 204, 150-167, 1998.

1093

1094 Smith, J.A. and Krajewski, W.F.: A modeling study of rainfall rate-reflectivity
1095 relationships, *Water Resour. Res.*, 29, 2505-2514, 1993.

1096

1097 Smith, J.A., Seo, D.J., Baeck, M.L., and Hudlow, M.D.: An intercomparison study of
1098 NEXRAD precipitation data, *Water Resour. Res.*, 32, 2035-2045, 1996.

1099

1100 Soong, D.T., Ishii, A.L., Sharpe, J.B., and Avery, C.F.: Estimating flood-peak discharge
1101 magnitudes and frequencies for rural streams in Illinois, U.S. Geological Survey
1102 Scientific Investigations Report 2004-5103, 162 p., 2004.

1103

1104 Stedinger, J.R., Vogel, R.M., and Foufoula-Georgiou, E.: Frequency Analysis of Extreme
1105 Events, in: D.R. Maidment (Eds.), *Handbook of Hydrology*, Chapter 18, 1993.

1106

1107 Troch, P.A., Smith, J.A., Wood, E.F., and de Troch, F.P.: Hydrologic controls of large
1108 floods in a small basin: central Appalachian case study, *J. Hydrol.*, 156, 285-309, 1994.

1109

1110 Veneziano, D., Moglen, G.E., Furcolo, P., Iacobellis, V.: Stochastic model of the width
1111 function, *Water Resour. Res.*, 36, 1143-1157, 2000.

1112

1113 Vivoni, E.R., Entekhabi, D., Bras, R.L., and Ivanov, V.Y.: Controls on runoff generation
1114 and scale-dependence in a distributed hydrologic model, *Hydrol. Earth Sys. Sc.*, 4, 983-
1115 1029, 2007.

1116

1117 Vogel, R.M., and Fennesset, N.M., Flow-duration curves I: New interpretation and
1118 confidence intervals, *J. Water Resour. Bull.*, 31, 6, 485-504, 1994.

1119

1120 Wallis, J.R., Schaefer, M.G., Barker, B.L., and Taylor, G.H.: Regional precipitation-
1121 frequency analysis and spatial mapping for 24-hour and 2-hour durations for Washington
1122 State, *Hydrol. Earth Syst. Sc. Discuss.*, 11, 415-442, 2007.

1123

1124 Wolman, M.G. and Costa, J.E.: Envelope curves for extreme flood events, *J. Hydraul.*
1125 Eng.-ASCE, Discussion, 110, 77-78, 1984.

1126

1127 Xie, H., Zhou, X., Hendricks, J.M.H., Vivoni, E.R., Guan, H., Tian, Y.Q., and Small,
1128 E.E.: Evaluation of Nexrad Stage III precipitation data over a semiarid region, *J. Am.*
1129 *Water Resour. As.*, 04055, 237-256, 2006.

1130

1131

1132

1133

1134

1135 **Tables**

1136 Table 1. Maximum rainfall intensity and Q_p for the Upper Colorado River Basin (UCRB)
 1137 and Lower Colorado River Basin (LCRB). Note that data are all sampled from time
 1138 intervals of measurement ≤ 2 hours.

RI	Area (km ²)	Intensity (mm h ⁻¹)		Q_p (m ³ s ⁻¹)	
		UCRB	LCRB	UCRB	LCRB
10	16	28.0 \pm 0.0	36.6 \pm 0.0	125 \pm 0	162 \pm 0
10	64	25.4 \pm 0.1	32.5 \pm 0.0	451 \pm 1	578 \pm 0
10	144	25.1 \pm 1.1	29.5 \pm 0.4	1004 \pm 44	1182 \pm 16
10	256	23.7 \pm 0.2	27.3 \pm 0.0	1682 \pm 13	1944 \pm 1
10	1024	19.8 \pm 1.5	19.7 \pm 0.4	5644 \pm 427	5610 \pm 114
10	1296	20.7 \pm 2.4	21.7 \pm 3.5	7439 \pm 873	7820 \pm 1268
10	4096	15.5 \pm 3.0	15.9 \pm 0.8	17682 \pm 3462	18134 \pm 890
10	11664	12.6 \pm 1.7	11.0 \pm 2.6	40914 \pm 5571	35521 \pm 8586
50	16	55.9 \pm 0.7	56.2 \pm 0.1	248 \pm 3	250 \pm 0
50	64	55.1 \pm 1.2	47.7 \pm 0.0	980 \pm 22	847 \pm 1
50	144	55.3 \pm 3.5	43.3 \pm 0.9	2211 \pm 142	1734 \pm 38
50	256	54.9 \pm 1.4	40.9 \pm 0.5	3901 \pm 101	2908 \pm 32
50	1024	50.8 \pm 5.5	33.6 \pm 1.4	14449 \pm 1569	9560 \pm 393
50	1296	50.8 \pm 25.0	32.5 \pm 3.9	18287 \pm 9011	11704 \pm 1410
50	4096	27.6 \pm 22.2	30.0 \pm 5.2	31382 \pm 25313	34126 \pm 5969
50	11664	21.1*	15.4 \pm 8.3	68434*	49764 \pm 26874
100	16	92.3 \pm 0.3	68.6 \pm 0.0	410 \pm 1	305 \pm 0
100	64	91.9 \pm 2.5	54.5 \pm 0.2	1635 \pm 44	970 \pm 3
100	144	90.1 \pm 3.0	51.9 \pm 1.0	3606 \pm 118	2075 \pm 41
100	256	88.7 \pm 4.3	48.4 \pm 0.4	6305 \pm 307	3440 \pm 27
100	1024	63.8 \pm 11.0	42.5 \pm 2.2	18155 \pm 3139	12085 \pm 630
100	1296	78.5 \pm 50.1	43.2 \pm 7.8	28257 \pm 18022	15544 \pm 2820
100	4096	40.8*	32.0 \pm 10.4	46422*	36425 \pm 11803
100	11664	21.1*	20.1*	68434*	65011*
500	16	254.0 \pm 0.8	81.9 \pm 0.5	1129 \pm 3	364 \pm 2
500	64	229.0 \pm 3.1	68.6 \pm 1.5	4071 \pm 55	1219 \pm 26
500	144	219.1 \pm 11.9	68.6 \pm 4.7	8762 \pm 476	2743 \pm 187
500	256	219.4 \pm 7.3	68.6 \pm 3.4	15600 \pm 517	4877 \pm 242
500	1024	166.0 \pm 44.1	68.6 \pm 3.1	47229 \pm 12554	19507 \pm 884
500	1296	174.6 \pm 85.3	65.6 \pm 31.3	62862 \pm 30696	23624 \pm 11279
500	4096	81.6*	53.6*	92844*	60930*
500	11664	21.1*	20.1*	68434*	65011*

1139 * Values with infinite confidence intervals, not used in this study.

1140

1141

1142

1143

1144

1145 Table 2. Maximum Q_{fd} for the Upper Colorado River Basin (UCRB) and Lower Colorado
 1146 River Basin (LCRB). Note that data are all sampled from time intervals of measurement
 1147 ≤ 2 hours.

RI	Area (km ²)	Wet Q_{fd} (m ³ s ⁻¹)		Med Q_{fd} (m ³ s ⁻¹)		Dry Q_{fd} (m ³ s ⁻¹)	
		UCRB	LCRB	UCRB	LCRB	UCRB	LCRB
10	16	65 ± 0	86 ± 0	36 ± 0	47 ± 0	20 ± 0	26 ± 0
10	64	246 ± 1	263 ± 0	137 ± 0	151 ± 0	75 ± 0	89 ± 0
10	144	465 ± 20	489 ± 7	268 ± 12	290 ± 4	156 ± 7	175 ± 2
10	256	657 ± 5	748 ± 0	388 ± 3	449 ± 0	244 ± 2	283 ± 0
10	1024	2363 ± 179	2194 ± 44	1423 ± 108	1326 ± 27	892 ± 68	820 ± 17
10	1296	2244 ± 263	2384 ± 387	1459 ± 171	1543 ± 250	1010 ± 118	1066 ± 173
10	4096	5594 ± 1095	5304 ± 260	3665 ± 718	3375 ± 166	2507 ± 491	2315 ± 114
10	11664	14603 ± 1966	11048 ± 2670	9010 ± 1213	6978 ± 1687	6105 ± 822	4942 ± 1195
50	16	131 ± 2	131 ± 0	73 ± 1	73 ± 0	41 ± 1	41 ± 0
50	64	553 ± 12	387 ± 0	307 ± 7	222 ± 0	172 ± 4	130 ± 0
50	144	1145 ± 73	720 ± 16	636 ± 41	424 ± 9	355 ± 23	259 ± 6
50	256	1772 ± 46	1119 ± 12	1043 ± 27	676 ± 7	639 ± 16	421 ± 5
50	1024	6127 ± 665	3062 ± 126	3665 ± 398	1928 ± 79	2291 ± 249	1308 ± 54
50	1296	7076 ± 3487	3562 ± 429	4265 ± 2102	2300 ± 277	2682 ± 1321	1571 ± 189
50	4096	15716 ± 12650	8487 ± 1485	9451 ± 7607	5850 ± 1023	6076 ± 4890	4343 ± 760
50	11664	44482*	15700 ± 8478	28783*	10176 ± 5495	19770*	7138 ± 3855
100	16	216 ± 1	160 ± 0	120 ± 0	89 ± 0	67 ± 0	50 ± 0
100	64	924 ± 25	442 ± 1	514 ± 14	255 ± 1	286 ± 8	150 ± 0
100	144	1807 ± 60	860 ± 17	1041 ± 35	508 ± 10	610 ± 20	309 ± 6
100	256	2888 ± 140	1324 ± 10	1706 ± 83	798 ± 6	1037 ± 50	499 ± 4
100	1024	10586 ± 1830	3812 ± 199	6366 ± 1101	2438 ± 127	3979 ± 688	1662 ± 87
100	1296	9564 ± 6100	4713 ± 855	5752 ± 3668	3058 ± 555	3619 ± 2308	2104 ± 382
100	4096	29415*	10319 ± 3344	19095*	6654 ± 2156	13116*	4698 ± 1522
100	11664	59600*	18607*	38667*	12904*	26747*	9609*
500	16	594 ± 2	192 ± 1	330 ± 1	107 ± 1	184 ± 1	59 ± 0
500	64	1855 ± 25	556 ± 12	1068 ± 14	320 ± 7	628 ± 8	188 ± 4
500	144	3631 ± 197	1138 ± 77	2141 ± 116	670 ± 46	1306 ± 71	408 ± 28
500	256	6012 ± 200	1879 ± 93	3618 ± 120	1130 ± 56	2266 ± 75	709 ± 35
500	1024	19049 ± 5059	6139 ± 278	11478 ± 3048	3945 ± 179	7186 ± 1909	2660 ± 120
500	1296	19075 ± 9314	7153 ± 3415	12370 ± 6041	4656 ± 2223	8499 ± 4150	3198 ± 1527
500	4096	43688*	14892*	28354*	10460*	19481*	7800*
500	11664	65705*	23062*	42738*	16198*	29364*	12080*

* Values with infinite confidence intervals, not used in this study.

1148

1149

1150

1151

1152

1153

1154

1155

1156

1157 Table 3. Maximum rainfall intensity and Q_p values for 10, 50, 100, and 500-year
 1158 recurrence intervals during negative (neg) and positive (pos) Multivariate ENSO Index
 1159 (MEI) conditions within the Lower Colorado River Basin (LCRB) and Upper Colorado
 1160 River Basin (UCRB). Note that data are all sampled from time intervals of measurement
 1161 ≤ 2 hours.

Basin	MEI	Area (km ²)	Intensity (mm h ⁻¹)				Q_p (m ³ s ⁻¹)			
			10 yr	50 yr	100 yr	500 yr	10 yr	50 yr	100 yr	500 yr
LCRB	neg	16	39	56	69	77	175	250	305	343
	neg	256	31	46	53	69	2206	3251	3741	4877
	neg	4096	21	32	43	54	23856	36425	48363	60930
	pos	16	40	64	74	130	179	284	330	576
	pos	256	27	38	47	52	1943	2690	3369	3721
	pos	4096	13	20*	20*	20*	15229	22689*	22689*	22689*
UCRB	neg	16	41	98	162	254	186	435	721	1129
	neg	256	33	101	155	254	2366	7172	11012	18055
	neg	4096	22	34	41	82	25556	39013	46422	92844
	pos	16	26	51	56	74	115	225	248	330
	pos	256	18	40	51	56	1255	2810	3601	4018
	pos	4096	10	26	27*	27*	10822	30034	31044*	31044*

1162 * Values with infinite confidence intervals, not used in this study.

1163

1164

1165

1166

1167

1168

1169

1170

1171

1172

1173

1174

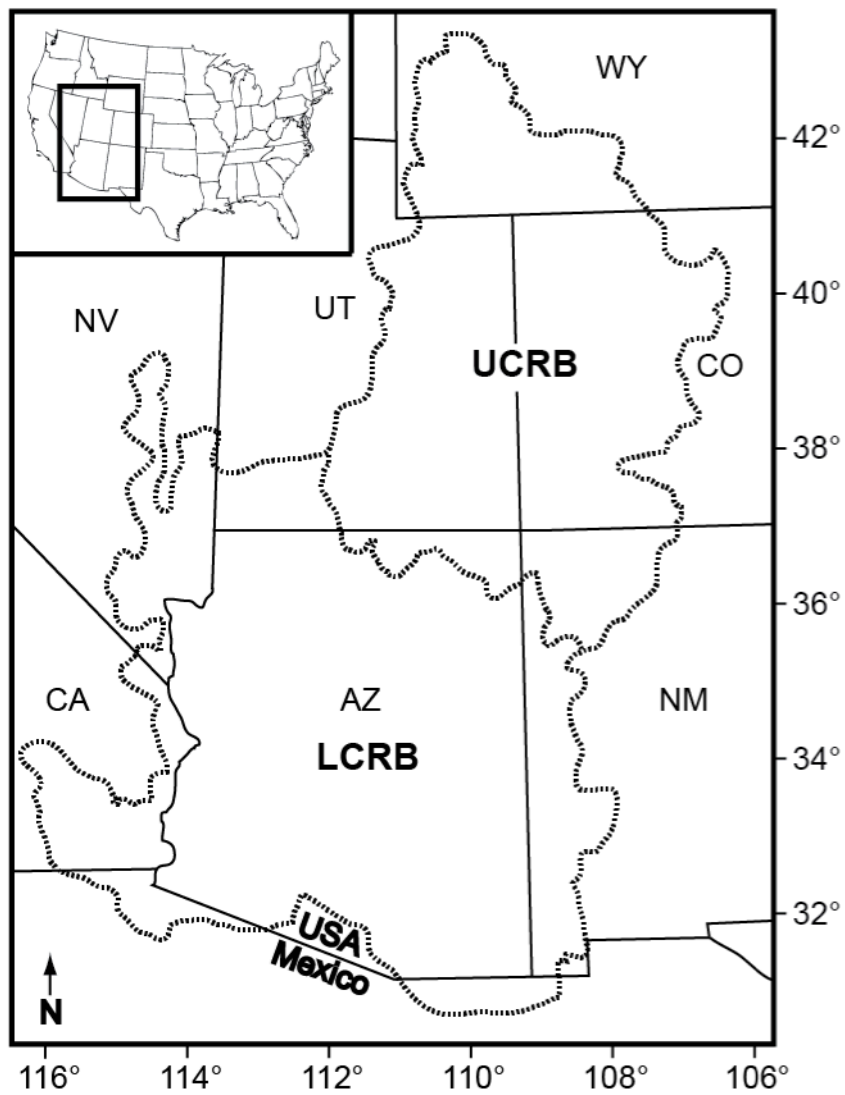
1175

1176

1177

1178

1179 **Figures**



1180

1181 Figure 1. Map showing the locations of the Upper and Lower Colorado River Basins
1182 (UCRB and LCRB, respectively) outlined by the dotted line.

1183

1184

1185

1186

1187

1188

1189

1190

A**Step 1: Rainfall Sampling Over Space and Time**

For "Time Interval" = 1, 2, 4, 8, 16, 32, 64 h

Rainfall = Average (Rainfall) into blocks of time of length "Time Interval" (see below)

For "Area" = 16, 64, 144, 256, 1024, 1296, 4096, 11664 km²

For "Basins" within drainage basin defined by user (see below)

For "Time" 1 to end of 9-year record in increments of "Time Interval"

Find max Rainfall in consecutive blocks of non-zero Rainfall a.k.a. storm event (see below)

n = count of max Rainfall values

Record max storm-event Rainfall ("Time Interval", "Area", n)

End For "Time" Loop

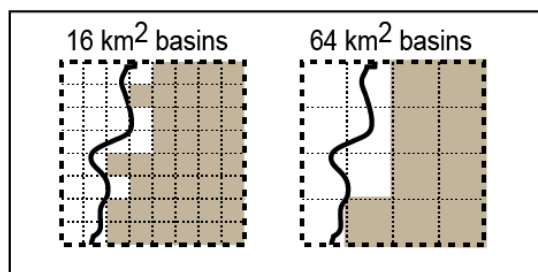
End For "Basins" Loop

End For "Area" Loop

End For "Time Interval" Loop

Result: 7 x 8 x n Array of Rainfall (Time Interval, Area, n)

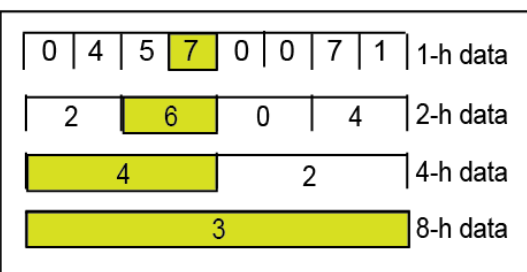
Example of gridded rainfall intensity
aggregated over spatial scales



— Study area outline

■ Basins included (within study area)

Example of rainfall intensity
averaged over temporal scales



■ Max Rainfall in Storm Event

Step 2: Rainfall Recurrence Interval Calculations

For "Time Interval" = 1, 2, 4, 8, 16, 32, 64 h

For "Area" = 16, 64, 144, 256, 1024, 1296, 4096, 11664 km²

Rank Rainfall from highest to lowest

For Recurrence Interval, "RI", = 10, 50, 100, 500 years

$m = (n + 1)/RI$ (see Equation 2)

Record Rainfall at rank m ("Time Interval", "Area", "RI")

End For "RI" Loop

End For "Area" Loop

End For "Time Interval" Loop

Result: 7 x 8 x 4 Array of Rainfall (Time Interval, Area, RI)

1191

1192 Figure 2A. Pseudocode describing the methods of the paper with schematic diagrams
1193 shown below pseudocode in some cases. Equations within the text and other figures are
1194 referenced in red text.

1195

1196

1197

B

Step 3: Q_{pm} Calculation

For Antecedent Moisture Condition, "AMC" = dry, medium, wet

For "Time Interval" = 1, 2, 4, 8, 16, 32, 64 h

For "Area" = 16, 64, 144, 256, 1024, 1296, 4096, 11664 km²

Runoff Coefficient, RC, set as function of "Area" (see Fig. 3)

For "RI" = 10, 50, 100, 500 years

$Q_p = \text{Rainfall} * \text{Time Interval} * \text{Area}$

$Q_{pm} = Q_p * RC(\text{AMC})$ (see Equation 3)

End For "RI" Loop

End For "Area" Loop

End For "Time Interval" Loop

End For "AMC" Loop

Find peak Q_{pm} value from all values for different time intervals and use as max Q_{pm} value

Result: 3 x 8 x 4 Array of Q_{pm} (AMC, Area, RI)

Step 4: Q_{fd} Calculation

For "AMC" = dry, medium, wet

For "Area" = 16, 64, 144, 256, 1024, 1296, 4096, 11664 km²

For "RI" = 10, 50, 100, 500 years

Slope, S, set as function of "Area" (see Figure 4A)

Channel Width, W, set as function of "Area" (see Figure 4B)

For "Iteration" = 1 to when water depth, h, change < 0.001

If "Iteration" = 1, then h = 1 m

Else when "Iteration" > 1, then h = last calculated h

Channel velocity, V = solve Manning's Equation (see Equation 4)

Drift velocity a = $(1+a_0)V$ (see Equation 6)

Diffusion coefficient b² = solve Diffusion Equation (see Equation 7)

For "Timestep" = 1 to end

For "Pixel" = 1 to channel length L

Q_{pm} added to 1D channel following triangular width function A(x)

Solve Unit Impulse Function q_{fd} (see Equation 5)

Record peak discharge Q_{fd} ("AMC", "Time Interval", "Area", "RI")

End For "Pixel" Loop

End For "Timestep Loop"

If h change < 0.001, then record peak Q_{fd} ("AMC", "Time Interval", "Area", "RI")

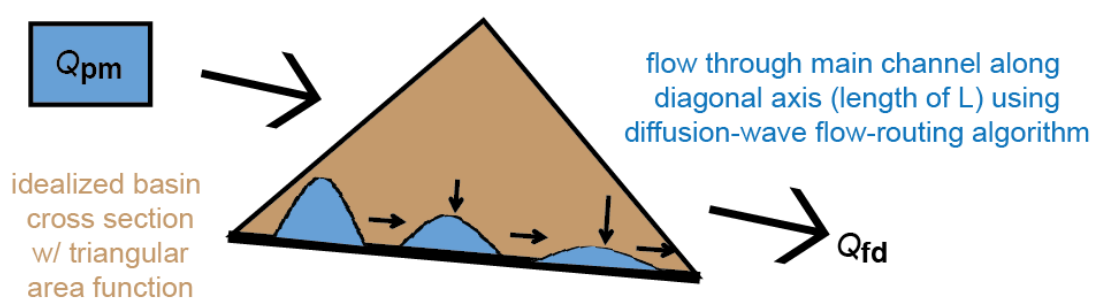
End for "Iteration Loop"

End For "RI" Loop

End For "Area" Loop

End For "AMC" Loop

Result: 3 x 8 x 4 Array of Q_{fd} (AMC, Area, RI)



1199 Figure 2B. Pseudocode describing the methods of the paper with schematic diagrams
1200 shown below pseudocode in some cases. Equations within the text and other figures are
1201 referenced in red text.

1202

1203

1204

1205

1206

1207

1208

1209

1210

1211

1212

1213

1214

1215

1216

1217

1218

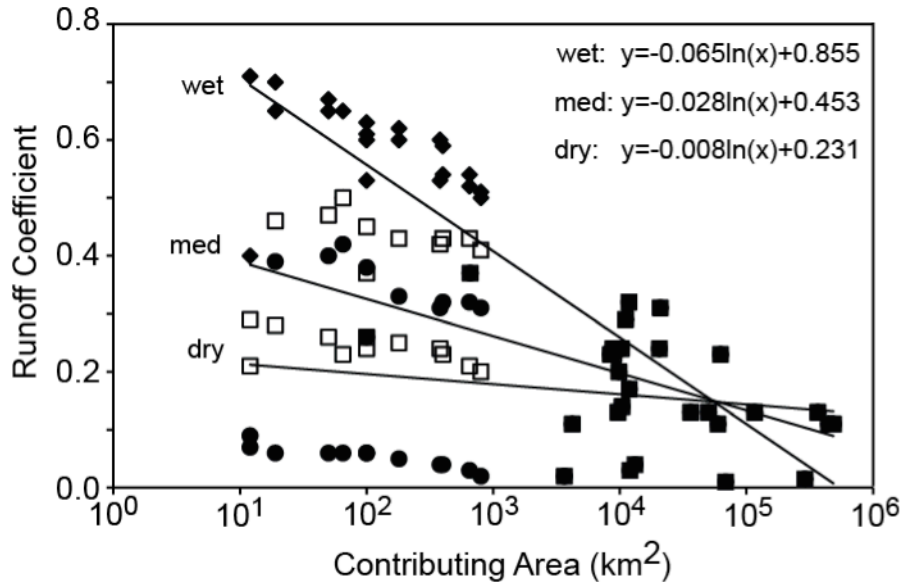
1219

1220

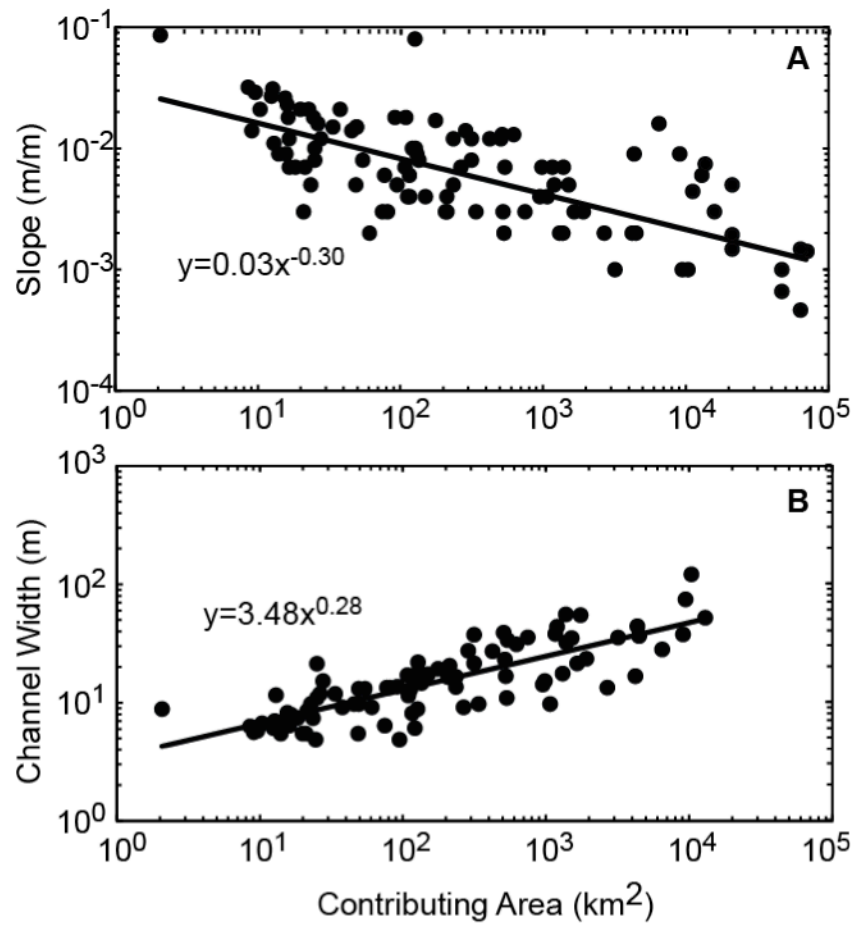
1221

1222

1223



1224
 1225 Figure 3. Logarithmic relationships between runoff coefficients and contributing area
 1226 using modeled data for wet (filled diamonds), medium (open squares), and dry (filled
 1227 circles) antecedent-moisture conditions (Vivoni et al., 2007) and measured data for larger
 1228 contributing areas (filled squares; Rosenburg et al., 2013). The medium (open squares)
 1229 and dry (filled circles) data separate into two distinct groups relating to the precipitation
 1230 event used to model them, with the lower group and higher group relating to a 12-h, 1-
 1231 mm h⁻¹ event and 1-h, 40-mm h⁻¹ event, respectively. All points were used in the least-
 1232 squares weighed-regression analysis.
 1233
 1234
 1235
 1236
 1237
 1238
 1239
 1240
 1241
 1242
 1243
 1244



1245

1246 Figure 4. Power-law relationships between channel slope and contributing area (A) and
 1247 channel width and contributing area (B) for the Colorado River Basin.

1248

1249

1250

1251

1252

1253

1254

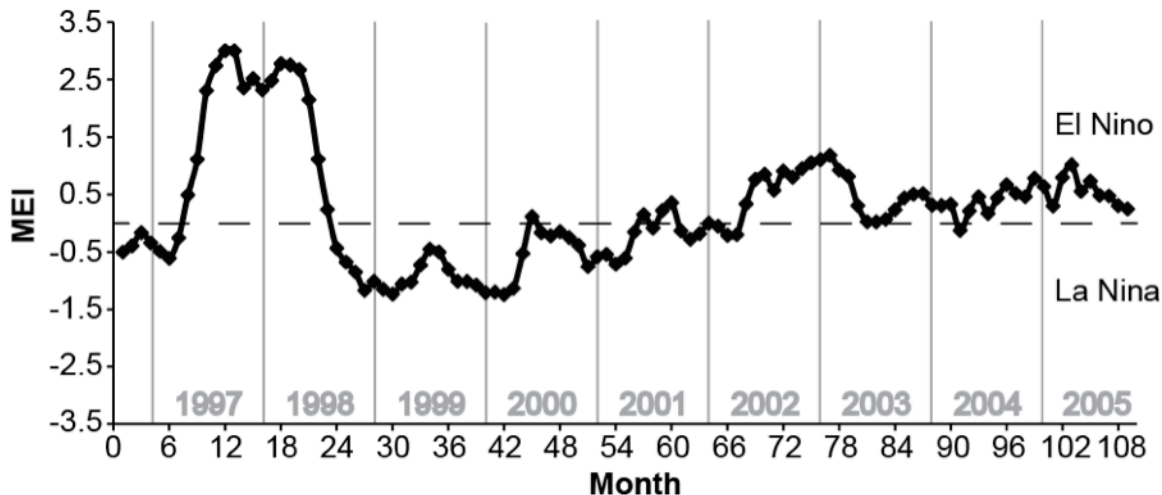
1255

1256

1257

1258

1259



1260

1261 Figure 5. Multivariate ENSO Index (MEI) of months included in Stage III NEXRAD
 1262 gridded products. Months are numbered from September 1996 to September 2005 with
 1263 years shown in gray. Dashed black line MEI equal to zero. Positive MEI indicates El
 1264 Niño conditions, while negative MEI indicates La Niña conditions.

1265

1266

1267

1268

1269

1270

1271

1272

1273

1274

1275

1276

1277

1278

1279

1280

1281

1282

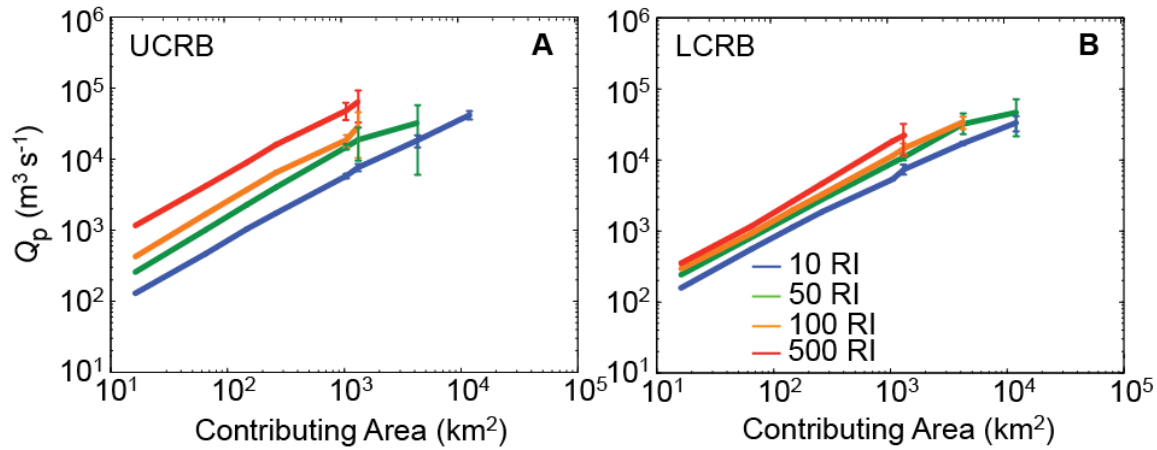
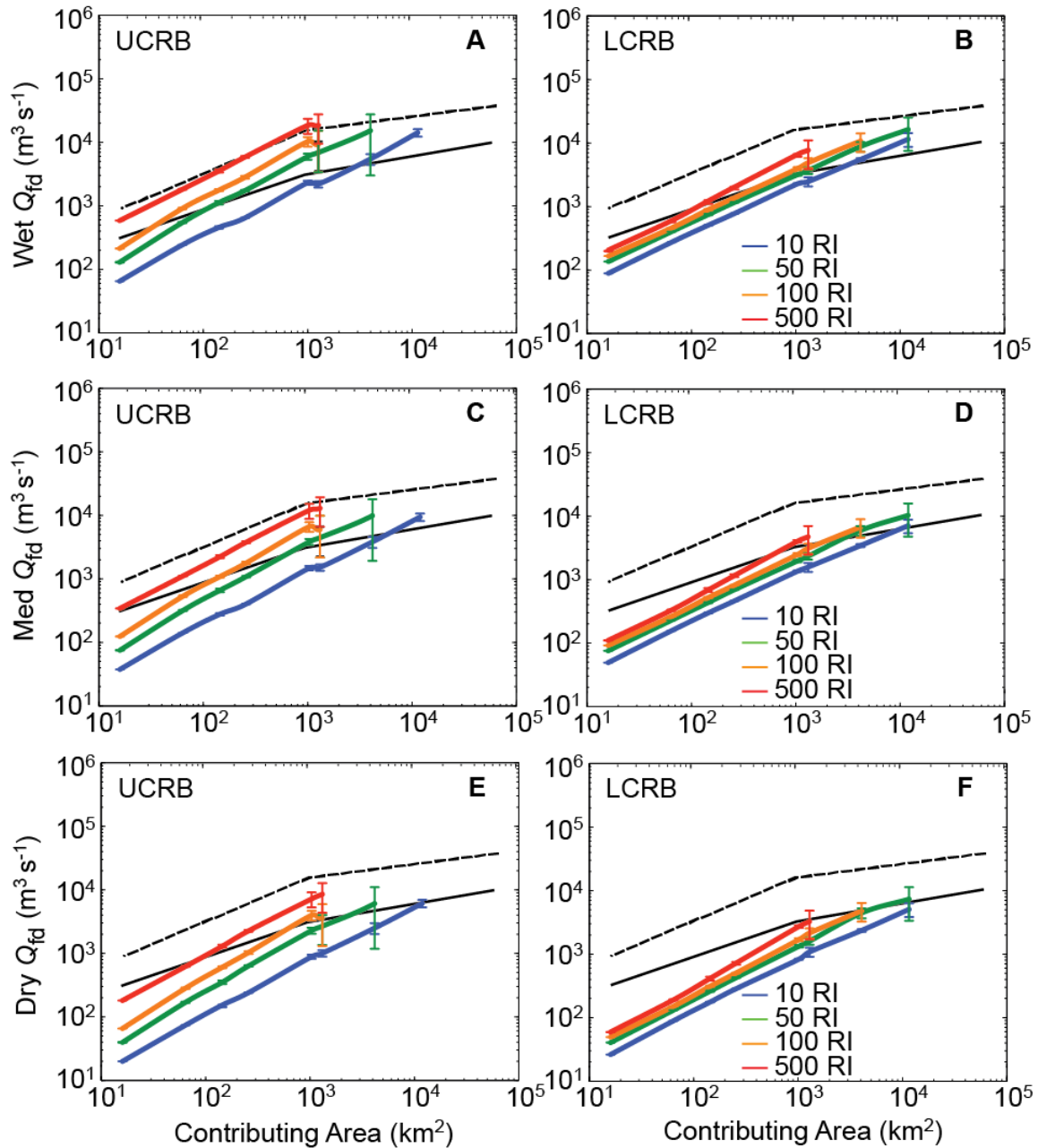


Figure 6. Frequency-magnitude-area (FMA) curves of Q_p versus contributing area for recurrence intervals (RI) of 10, 50, 100, and 500 years for the Upper Colorado River Basin (UCRB; A) and the Lower Colorado River Basin (LCRB; B).

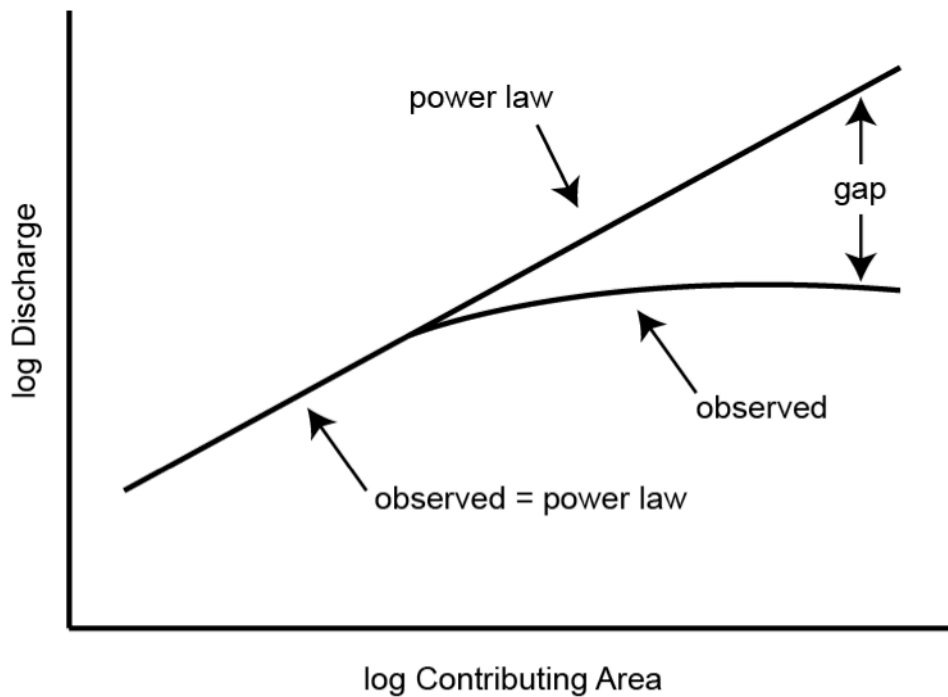


1307

1308 Figure 7. Q_{fd} frequency-magnitude-area curves of 10, 50, 100, and 500 recurrence
 1309 intervals (RI) and for wet, medium, and dry conditions for the Upper Colorado River
 1310 Basin (UCRB) and the Lower Colorado River Basin (LCRB). Published FECs (black
 1311 lines) for the Lower Colorado River Basin (solid black line) from Enzel et al. (1993) and
 1312 the United States (dashed black line) from Costa (1987) are also shown.

1313

1314



1315
 1316 Figure 8. Conceptual diagram of the characteristic concave-down shape of the FEC
 1317 (observed) shown in comparison to a power-law function between Q_p and contributing
 1318 area. The “gap” between the observed curve and the predicted power law is caused by
 1319 precipitation limitations and mechanisms occurring during the routing of water over the
 1320 landscape.

1321

1322